STUDIES OF JET FUEL AUTOXIDATION CHEMISTRY: CATALYTIC HYDROPEROXIDE DECOMPOSITION & HIGH HEAT FLUX EFFECTS

Dissertation

Submitted to

The School of Engineering of the

UNIVERSITY OF DAYTON

In Partial Fulfillment of the Requirements for

The Degree

Doctor of Philosophy in Mechanical Engineering

By

Zachary John West

UNIVERSITY OF DAYTON

Dayton, Ohio

December 2011

STUDIES OF JET FUEL AUTOXIDATION CHEMISTRY: CATALYTIC HYDROPEROXIDE DECOMPOSITION & HIGH HEAT FLUX EFFECTS

Name: West, Zachary John

APPROVED BY:

Jamie S. Ervin, Ph.D.
Advisory Committee Co-Chairman
Professor
Mechanical & Aerospace Engineering

Steven S. Zabarnick, Ph.D.
Advisory Committee Co-Chairman
Distinguished Research Chemist
University of Dayton Research Institute
Professor
Mechanical & Aerospace Engineering

Dilip Ballal, Ph.D.
Committee Member
Professor
Mechanical & Aerospace Engineering

James T. Edwards, Ph.D.
Committee Member
Senior Chemical Engineer
Air Force Research Laboratory

John G. Weber, Ph.D.
Associate Dean
School of Engineering

Tony Saliba, Ph.D.
Dean, School of Engineering
& Wilke Distinguished Professor

ABSTRACT

STUDIES OF JET FUEL AUTOXIDATION CHEMISTRY: CATALYTIC HYDROPEROXIDE DECOMPOSITION & HIGH HEAT FLUX EFFECTS

Name: West, Zachary John
University of Dayton

Co-Advisors: Drs. J. S. Ervin & S. Zabarnick

Jet fuel has been used as an aircraft and engine coolant for decades. However, one problem associated with heating the fuel is the occurrence of deposition reactions that foul critical fuel system components. If left unchecked, these fuel system deposits can cause catastrophic failure. The chemical pathways leading to fuel oxidation and deposition are not fully understood. In order to better understand these pathways, the kinetic parameters of hydroperoxide decomposition, relevant to jet fuel oxidation, have been measured in the presence of potential homogeneous catalytic sources, i.e., dissolved metals and naphthenic acids. The addition of dissolved metal alone was found to increase the decomposition rate of hydroperoxides, while the addition of naphthenic acids alone was found to have little effect on the rate. However, the combination of dissolved metal and naphthenic acids is shown to synergistically increase the decomposition rate of hydroperoxides. The catalytic effect of metal and naphthenic acids on real fuel deposition rates was explored, and in general followed similar trends to the hydroperoxide rate data.

Separate thermal oxidation experiments were conducted with jet fuel to explore advanced cooling schemes, e.g., regenerative cooling. Regenerative cooling schemes are often characterized by large heat fluxes and high wetted wall temperatures. Due to the complex experimental fluid flows and severe heat transfer conditions, computational fluid dynamics (CFD) with chemistry was used to predict chemical reaction rates and species concentrations. Some of the resulting kinetic data for hydroperoxide decomposition was incorporated into a revised pseudo-detailed chemical kinetic model, which was used in the CFD with chemistry computations. The relatively severe heat transfer conditions: heat fluxes of 0.26 and 0.49 Btu/s-in^2 (43 and 81 W/cm^2), wall temperatures of up to about 660°C, and bulk fluid temperatures as low as 27°C, caused the formation of large radial thermal gradients. In one case, heating of the fuel was sufficient to transition the flow from laminar to turbulent, which enhanced the reaction rate for some reactions. The large thermal gradients and high wall temperatures, coupled with flow conditions, created unique zones of chemical activity within the flow field. These zones of chemical activity included the localized depletion of dissolved oxygen within the boundary layer. CFD with chemistry was able to provide spatial resolution to the complex flow field to assist with experimental analysis.

DEDICATION

To my children, Aiden and Eleanor, I hope you both find joy and inspiration in life.

ACKNOWLEDGEMENTS

First, I thank my advisory committee members for their time and wisdom, but mostly Drs. Steve Zabarnick and Jamie Ervin for their patience and guidance with me over the years. I must also thank my many wonderful co-workers at UDRI and AFRL especially: Mr. Rich Striebich and Dr. Matt DeWitt, for entertaining and sometimes useful discussions; Mrs. Linda Shafer and Mrs. Rhonda Cook, for the enormous volume of high quality analysis the two of you perform, even with the amount of turmoil and agony you must endure from the rest of us; Dr. Hua Jiang, Mr. Ted Williams, and Mr. Joe Mantz, for contributing useful data and useful discussions; and Mr. Ryan Adams and Ms. Milissa Flake, for also contributing useful data and sometimes useful distractions.

I also thank my family and friends for their unending support, and unending nagging of me to get this done. My utmost thanks and appreciation, however, is reserved for my wonderful accomplice in life, Alicia.

This material is based on research sponsored by the U.S. Air Force Research Laboratory under agreement numbers: F33615-03-2-2347 and FA8650-10-2-2934. The U.S. Government is authorized to reproduce and distribute reprints for Governmental purposes notwithstanding any copyright notation thereon.

TABLE OF CONTENTS

CHAPTER

APPENDICES

LIST OF FIGURES

LIST OF TABLES

LIST OF SYMBOLS & ABBREVIATIONS

A	Arrhenius frequency factor (mole, L, s)
A•	alkyl-phenol radical
AFRL	United States Air Force Research Laboratory
AH	alkyl-phenol species
API	American Petroleum Institute
CFD	computational fluid dynamics
CHP	cumene hydroperoxide
C_p	constant pressure specific heat capacity (kJ/kg-K)
CRC	Coordinating Research Council
D	mass diffusivity (m^2/s)
DHP	n-dodecane hydroperoxide
E_a	activation energy (kcal/mole)
EBHP	ethylbenzene hydroperoxide
f	crystal frequency (MHz)
f_o	initial crystal resonant frequency (MHz)
GC-FID	gas chromatography with flame ionization detector
GC×GC	comprehensive two-dimensional gas chromatography
Gr	Grashof number (dimensionless)
H	specific enthalpy (kJ/kg)

HPLC-MS	high performance liquid chromatography with mass spectrometer detector
I	initiator species
k	Arrhenius reaction rate constant (mol, L, s)
k	thermal conductivity (W/m^2-K)
k_o	pseudo-first order rate constant of hydroperoxide thermal decomposition without metal
M	dissolved metal species
MDA	metal deactivator additive [N,N’-Bis(salicylidene)-1,2-propanediamine]
mM	millimolar (mmol/L)
NA	naphthenic acids
NIST	National Institute of Standards and Technology
Nu	Nusselt number (dimensionless)
ppb	parts per billion (unless otherwise specified: µg/kg)
ppm	parts per million (unless otherwise specified: mg/kg)
Products_{AH}	deposit precursor species from alkyl-phenol species
Products_{SH}	deposit precursor species from reactive sulfur species
$\dot{q}$	power (Btu/s or W)
q'''	volumetric energy source term (Btu/s-in^3 or W/m^3)
QCM	quartz crystal microbalance
R•	hydrocarbon radical
R^2	coefficient of determination
Re	Reynolds number (dimensionless)
RH	hydrocarbon species
RNG	renormalized group κ-ε turbulence model

$RO_2\bullet$	peroxy radical
RO_2H	hydroperoxide species
RSD	relative standard deviation
RSM	Reynolds stress model
Sc	Schmidt number (dimensionless)
SH	reactive sulfur species, e.g., thiol, sulfide, and disulfide
SIMPLEC	semi-implicit method for pressure-linked equations – consistent
SKE	standard κ-ε turbulence model
SST	shear-stress transport
St	Stanton number (dimensionless)
TAN	total acid number (mg KOH/g)
T_{pc}	pseudo-critical temperature (°C)
UDRI	University of Dayton Research Institute
α	thermal diffusivity (m^2/s)
ε	turbulence dissipation rate (m^2/s^3)
κ	turbulent kinetic energy (kJ/kg)
μ	viscosity (cP)
ρ	density (kg/m^3)
ρ_s	surface mass density ($\mu g/cm^2$)
τ	residence time (s or m^2/m^2-s or m^3/m^3-s)
ω	specific turbulence dissipation rate (s^{-1})

CHAPTER I

INTRODUCTION

Background

Turbine engine aircraft have used a kerosene distillate fraction as a propellant since the early stages of their development and use (Davies, 2003; Edwards, 2003). The turbine engine was considered to be insensitive to the type of fuel it combusted, and the decision to use kerosene as a jet fuel came about mostly due to the strategic availability of fossil fuel based kerosene during World War II (Edwards, 2003; Martel, 1987). In addition to availability, kerosene fuels exhibited some favorable physical and chemical properties such as low freeze point and reliable high-altitude relight (Dukek et al., 1969). Increases in aircraft speed and the subsequent increases in aircraft heat load brought on the need to use jet fuel as a coolant for various equipment and subsystems, e.g., lubricant system, hydraulic system, electronics, and environmental control system. Today, jet fuels are one of the most highly specified finished fuels available.

Using jet fuel as a heat sink is a beneficial strategy to mitigate excess heat. However, it was quickly discovered that higher fuel system temperatures encouraged carbon deposits within the fuel system (Schwartz & Eccleston, 1962). Problems stemming from these carbon deposits include, for example: fouled heat exchangers, plugged fuel filters, occluded flow passages, and valve hysteresis. All of these problems force a more rigorous aircraft maintenance cycle which is costly in both time and money. Yet if left unchecked, the effects of fuel system fouling can be catastrophic for an aircraft and crew. As a result, current jet fuel standards require a minimum specification level of thermal stability for both military, JP-5/JP-8, and civilian, Jet A/A-1, grades of fuel (MIL-DTL-5624U; MIL-DTL-83313G; ASTM D1655-11a). However, future aircraft heat sink demands are increasing and the need for high thermal stability fuels is ever present (Edwards, 2003). The current understanding of jet fuel instability – the causes, the measurement of, and the prediction of – is still incomplete. Investigation of jet fuel stability continues to be an important area of research.

Jet Fuel Stability

Jet fuel stability can be classified into three regimes: storage stability, thermal-oxidative stability, and pyrolytic stability. Storage stability addresses the ability of a jet fuel to resist chemical oxidation over months or years of storage under ambient conditions. Ambient storage temperatures are less severe (typically about -20 to 60°C) than aircraft conditions. However, there is an abundant supply of dissolved oxygen – and time – during storage, which promotes fuel degradation reactions. Oxygenated species, e.g., hydroperoxides and carboxylic acids, formed during jet fuel storage can impact ground handling equipment by attacking materials. These oxygenated species, and other contaminants introduced during storage due to material deterioration, can have a negative effect on the future thermal stability of the fuel.

Thermal-oxidative stability refers to the ability of a jet fuel to withstand deposition reactions due to fuel oxidation under the typical thermal stresses imposed by aircraft heat loads and flow conditions. These fuel temperatures are much higher than storage conditions (about 100 to 350°C), yet the dissolved oxygen in the fuel system lines is limited to the air saturated amount of about 70 ppm (1.8 mM) oxygen in fuel (Striebich & Rubey, 1994). Actual thermal stress conditions are highly aircraft and mission dependant, with high Mach, high performance aircraft, e.g., military fighter jet aircraft, experiencing some of the highest fuel temperatures and heat loads. Maximum fuel temperature and total heat load are not the only indicators of when the thermal stability of jet fuel may be an issue. A survey of commercial aircraft engine conditions was conducted by the Coordinating Research Council (CRC, 1991) and the results indicated maximum design fuel temperatures of 120 to 150°C were being used. Fuel residence times at these maximum temperatures were not reported; however, it was expressed that maximum temperatures are attained within the fuel nozzle region where residence times are "very short" (about 0.1 to 1 s). Fuel nozzles are an area of concern for carbon deposits, but this CRC report (1991), and a previous CRC report (1979), both indicate that fuel control valves, actuators, and their protective screens were also a critical engine component of concern. Valve sticking and hysteresis due to carbon deposits is possible because of the small valve operating clearances (~0.001 inch), long relative fuel residence times (about 1 to 20 s), and elevated (but not maximum) temperatures (CRC, 1991; Hazlett, 1991).

The importance of residence time and temperature on jet fuel thermal-oxidative stability has been emphasized by others (CRC, 1991; Hazlett, 1991; Zabarnick, 1994). Jet fuel oxidation and deposition reactions follow an Arrhenius rate behavior, which can be approximated by a global reaction. For example, a zero order global oxidation reaction can be used to model the reaction timescales of an oxidizing jet fuel, with an activation energy of E_a = 35.8 kcal/mol and Arrhenius parameter of A = 2.2×10^{11} mol/L-s, as reported by Jones et al. (1993). Figure 1 shows a plot of the resulting reaction timescale versus fuel temperature for a global oxidation reaction using these empirical Arrhenius parameters assuming a 90% reduction in dissolved oxygen from an initial concentration of 70 ppm. The figure shows that a residence time of about 900 seconds is required to consume 90% of the dissolved oxygen at a fuel temperature of 150°C, but only 10 seconds is required to consume an equivalent amount of oxygen at 200°C. These timescales are relevant to real aircraft as flowing jet fuel is exposed to high engine temperatures for tens of seconds during a single pass through the fuel control loop, and potentially longer residence times for multi-pass fuel control systems (Dieterle & Binns, 1998; Hazlett, 1991).

Jet fuel pyrolysis involves the decomposition of bulk fuel hydrocarbons into smaller molecular weight species. This decomposition process involves the breaking of high energy carbon-carbon bonds. For example, Ward et al. (2005) reported an E_a = 63 kcal/mol and an A = 1.6×10^{15} s^{-1} for the first order pyrolysis of n-decane, which was used as a jet fuel surrogate. This first order, global pyrolytic reaction is used to illustrate the approximate timescales of 25% fuel pyrolytic conversion with the results shown in Figure 1. As the figure shows, when fuel temperatures are greater than about 500°C the reaction proceeds at times ≤ 100 s, which again are relevant to real fuel systems.

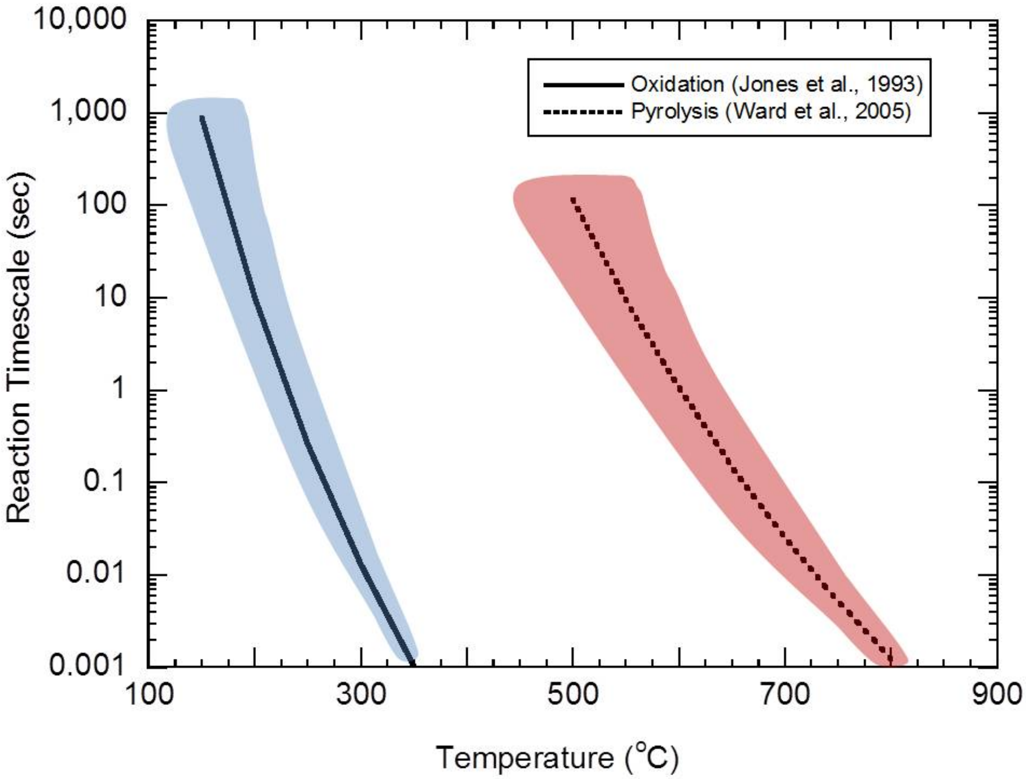

Figure 1. Reaction timescales for global oxidation (solid curve) and global pyrolytic (dashed curve) models; blue and red zones indicate the notional variability of real fuels in oxidative and pyrolytic reactivity, respectively.

Jet Fuel Chemistry

The chemical composition of jet fuel is an influential factor with respect to the stability of a fuel. Jet fuel is comprised of hundreds to thousands of individual species, most of which are hydrocarbons containing eight to sixteen carbons per molecule. The bulk hydrocarbon species account for about 99% of the total fuel composition and include mostly normal-, iso-, & cyclo-alkanes, and alkyl-aromatics. Indigenous trace chemical species, e.g., heteroatomic sulfur, nitrogen, and oxygenated species, dissolved metals, molecular oxygen, and water constitute the remaining 1% of jet fuel. Trace chemical species have been shown to greatly influence the storage and thermal-oxidative stability of jet fuel, while bulk chemical species impact mostly physical properties, e.g., density and viscosity, and some chemical properties such as pyrolytic stability (Hazlett, 1991; Schwartz & Eccleston, 1962). In addition, military grade jet fuels contain property enhancing additives such as static dissipater additive (SDA), fuel system icing inhibitor (FSII), and corrosion inhibitor/lubricity improver (CI/LI).

Autoxidation Mechanism

In order to predict the chemical behavior of fuels for design purposes it is important to develop chemical kinetic mechanisms. Many schemes have been used to model the complex chemical kinetics involved with hydrocarbon autoxidation, pyrolysis, and/or combustion such as global, detailed, and pseudo-detailed mechanisms (Katta et al., 1998; Ranzi et al., 2001; Zabarnick, 1998). The global modeling approach masks the actual chemical mechanisms in order to simplify the problem. Additionally, these models tend to simply fit experimental data and are difficult to extrapolate to other conditions and systems due to the inherent lack of chemically meaningful reactions and rate parameters. In contrast, the development of detailed chemical kinetic mechanisms provides the greatest chemical realism and allows extrapolation to a range of conditions, but their use is intractable for real fuel mixtures due to the complexity of real fuels, i.e., thousands of individual chemical species each participating in hundreds of reactions, with limited computational resources to solve such demanding systems. The combustion community has often used the knowledge of fundamental reaction pathways and applied this knowledge to a more comprehensive “lumped” model using species class reactions rather than individual ones (Ranzi et al., 2001; Curran et al., 1998). In a similar way, the problem of liquid phase jet fuel autoxidation has been studied using pseudo-detailed oxidation mechanisms (Zabarnick, 1998). The pseudo-detailed oxidation mechanism combines certain bulk and trace species into classes and is believed to strike a useful balance between the global and detailed modeling approaches. These pseudo-detailed mechanisms retain the chemical fidelity of the detailed mechanisms, yet are small enough to be readily employed into CFD simulations. Pseudo-detailed mechanisms have been used successfully to predict jet fuel oxidation and deposition over a range of fuel samples, temperatures, and flow regimes (Kuprowicz et al., 2007). Yet more refinement to these pseudo-detailed mechanisms, by both experimental validation and expanded chemical knowledge, is desired especially regarding the catalytic effects of metals and the decomposition pathways of hydroperoxide intermediates. To achieve this refinement, pseudo-detailed models rely upon focused experimental and computational studies of specific reaction pathways that involve classes of chemical species.

It is generally accepted that jet fuel autoxidation proceeds via a free radical chain mechanism, like that reported recently by Kuprowicz et al. (2007), and shown schematically in Figure 2. The RH in the figure represents a jet fuel hydrocarbon species, R• and RO_2• are the subsequent hydrocarbon radical and peroxy radical, respectively, RO_2H is a hydroperoxide, AH is a phenolic species, and SH is a reactive sulfur species. Hydroperoxides are the primary product of autoxidation at lower temperatures, ≤120°C; however, they decompose at higher temperatures to form radicals which auto accelerates the oxidation process. Hydroperoxides may also react with other heteroatomic species in fuels, e.g., sulfides and disulfides, to form non-radical products (Figure 2) that have been implicated as deposit precursors (Jones et al., 1996; Mushrush et al., 1996). Dissolved metals and organic acids present in jet fuel are thought to catalyze the homolytic, i.e., radical forming, hydroperoxide decomposition pathways.

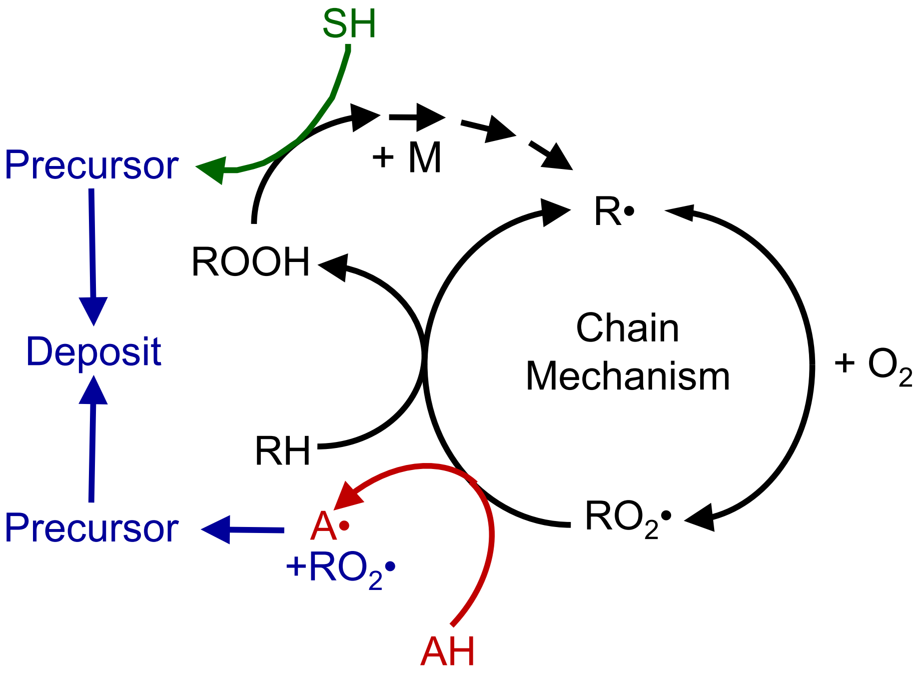

Figure 2. Diagram of the autoxidation chain mechanism for jet fuel (Kuprowicz et al., 2007).

While hydrocarbons do not readily solubilize metal ions directly, trace amounts of dissolved metal are present in jet fuel with the aid of naturally occurring organic ligands. The exact forms of these organic ligand species are not well known; however, the most likely is a mixture of carboxylic acids, e.g., naphthenic acids (Hazlett, 1991). Fuel contacts various metal components in the production and supply chains, which can bind with the naphthenic acids in the fuel to form fuel soluble metal naphthenates. Even with limited solubility, ppb to low ppm levels of metals have been shown to impact the thermal oxidative stability of jet fuels by increasing the overall oxidation rate and/or increasing the deposition tendency of a given fuel (Hazlett, 1991). Experiments investigating the impact of metals on the thermal stability of fuel have generally concentrated on the net effects of oxidation and/or deposition from a global viewpoint, with few studies focusing on the direct impact of these metals on any one mechanistic step.

Accumulation of organic acids, due to the oxidation of fuel hydrocarbons, can occur during the storage and handling of fuels. These carboxylic acids can be corrosive to some metals and help make these metals more soluble in fuel. Organic acids have been shown to increase fuel deposition and are typically considered to have a negative impact on fuel thermal stability and material compatibility (Hazlett, 1991). However, the effect these organic acids have on fuel hydroperoxides is not well understood. While many studies of acid catalyzed hydroperoxide decomposition can be found in the literature, the experimental conditions typically involve high reactant concentrations, strong acids, and non-hydrocarbon solvents (Kharasch et al., 1950; Kharasch et al., 1951; Kharasch & Burt, 1951; Petrov et al., 1977). These conditions are unlike the conditions experienced in a typical jet fuel environment where low reactant concentrations are expected due to the low dissolved oxygen content. Moreover, specification tests such as ASTM D3242 for total acid number (TAN) and ASTM D381 for existent gums are designed to alert the jet fuel user of excessive oxidation during storage. Therefore, accumulation of oxygenated products during storage should be minimized when specification fuels are used. For example, the TAN is limited to a maximum concentration of only 0.015 mg KOH/g (about 0.2 mM) for specification JP-8 jet fuels (MIL-DTL-83133G). Also, the acids generated during fuel oxidation are weak organic acids, not the strong mineral acids often studied as catalyzing reagents. Additionally, it has been shown that non-polar, hydrocarbon solvents tend to encourage homolytic reaction pathways and suppress heterolytic pathways, i.e., ion producing decompositions (Gao et al., 2002). This is in contrast to polar solvents that encourage heterolytic reactions. Previous studies investigating catalysis of hydroperoxides conducted in polar solvents hold only limited relevance to the chemical pathways in jet fuel.

There is mounting evidence that questions the role of dissolved metals as true catalysts in jet fuel; a catalyst being a compound that lowers the activation energy of a reaction while remaining unchanged/unconsumed by the reaction itself. Zabarnick and Phelps (2006) reported the homolytic decomposition of hydroperoxide is believed to have no activation energy barrier, E_a; thus, the reaction cannot be catalyzed since there is no energy barrier to lower. The reduced E_a of metal "catalyzed" hydroperoxide decomposition could be due to a lower energy pathway forming different radical products, such as the formation of a new metal complex. Additionally, Morris et al. (2005) have reported that dissolved copper tends to be removed from the fuel during autoxidation and concentrates in carbonaceous deposits. Thus the copper is actually being consumed during thermal oxidation rather than being regenerated like a true catalyst. It might be more accurate to say that hydroperoxide decomposition can be metal assisted rather than catalyzed.

Deposition Mechanism

As Figure 1 shows, the autoxidation of jet fuel occurs on relevant timescales from about 150 to 350°C, and the resulting oxidative deposition pathways proceed similarly. Figure 3 illustrates this deposition regime as a function of temperature provided sufficient residence time is allowed for fuel deposition reactions to proceed. By the time jet fuel is heated to about 350°C the reaction timescale for oxidation is so small (milliseconds) that oxygen is consumed almost instantaneously for most engineering practices. When this limiting reactant, i.e., oxygen, is fully consumed, oxidative deposition decreases since deposit precursors are no longer being formed. After oxygen is fully consumed, but before pyrolytic reactions become significant (typically at fuel temperatures between about 350 to 500°C), there is a region of little deposition activity. At much higher temperatures, ≥ 500°C, jet fuel pyrolysis and pyrolytic deposition begin to occur on relevant timescales.

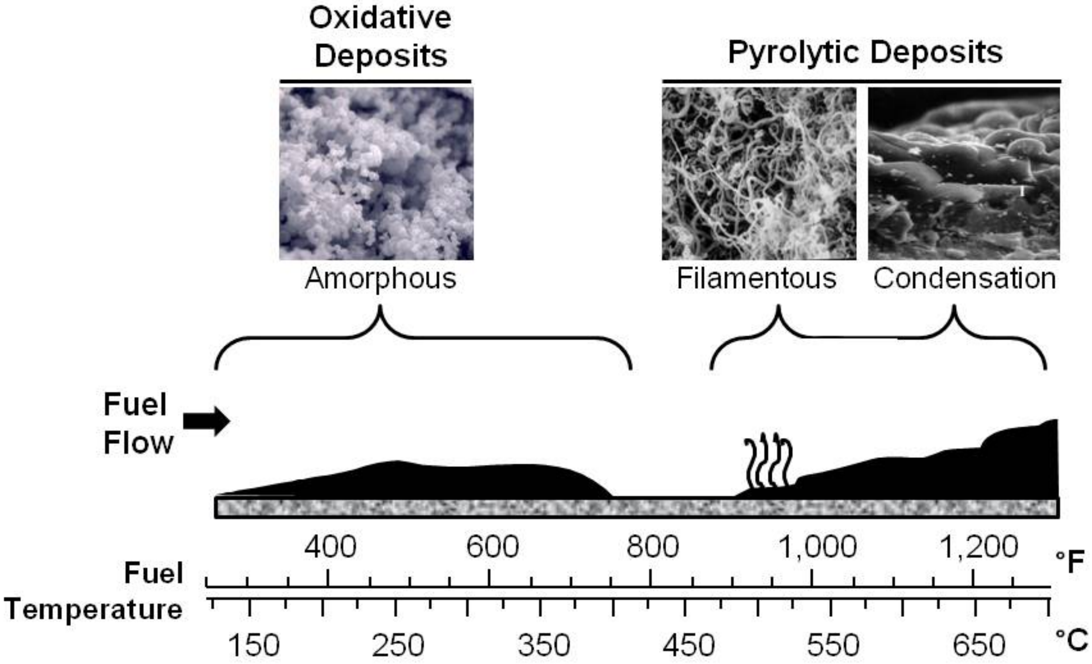

Figure 3. Jet fuel deposition regimes (Edwards, 2003; Kuprowicz, 2006).

The composition of jet fuel oxidative deposits has been well studied and Table 1 lists the typical ranges of elemental composition for these deposits, along with the concentration factors for nitrogen, sulfur, and oxygen (Hazlett, 1991). The concentration factor is the ratio of the elemental composition found in solid deposits to the elemental composition found in the bulk fuel. The very large concentration factors for the heteroatomic species, from the fuel into the deposit, highlight the importance of these species in deposition pathways.

Table 1. Composition of Oxidative Deposits (Hazlett, 1991)

Element	Composition (wt %)	Concentration Factor
Carbon	30 – 80	
Hydrogen	2 – 10	
Nitrogen	0 – 5	0 – 300,000
Sulfur	0 –10	0 – 2,500
Oxygen	10 –25	1,500 – 3,600
Ash	0 –35	

Previous studies have examined specific chemical reactions involved in jet fuel oxidative deposition (Hardy & Wechter, 1994; Beaver et al., 2005; Kauffman, 1997). The studies of Hardy and Wechter (1994) and Beaver et al. (2005) suggest a polymerization pathway of oxidation products and heteroatomic nitrogen species to produce carbonaceous deposits. Kauffman (1997) suggests a more complex deposition pathway that involves hydroperoxides, reactive sulfur species, and heteroatomic nitrogen species. Still others have proposed that polymerization of jet fuel oxidation products must also be accompanied by a series of physical processes, i.e., agglomeration of polymerized molecules, collection of agglomerated particles on surfaces, followed by particle coalescence and plastic flow, for deposition to occur on surfaces (Taylor, 1979). Regardless, many complex deposition pathways exist; and therefore, oxidative deposition is often modeled using a global approach for simulating deposition (Giovanetti & Szetela, 1985; Katta & Roquemore, 1993; Ervin et al., 1996). Recent works have successfully used a lumped approach to model oxidative deposition for bulk fuel temperatures up to about 360°C (Kuprowicz et al., 2007). The lumped approach to deposition modeling is more specific than global models and allows *a priori* prediction of deposition based on species class measurements.

Jet Fuel and Heat Transfer

Turbine aircraft components were initially air cooled often by re-routing a small air stream, called "bleed air," from the engine compressor. However, as compressor pressure ratios and air flight speeds both increased, so did the compressor air exit temperatures. This resulted in bleed air that was too hot to cool engine components, so fuel became a primary coolant. Unfortunately, when jet fuel degrades as it is heated the resulting carbon surface deposits foul heat exchange surfaces. Carbon surface deposits have a low thermal conductivity, 0.07 Btu/h-ft-°F (Hazlett, 1991), especially compared to common materials used in heat exchanger construction such as: copper, alumina, and superalloy with thermal conductivities of 210, 3.5, and 13 Btu/h-ft-°F, respectively (Edwards, 2003). Fuel system fouling inhibits efficient heat transfer which leads to hotter material temperatures and potentially catastrophic component failure. This is especially true for situations where a constant, high heat flux is present, such as in hypersonic aircraft combustors. For example Heiser and Pratt (1994) have estimated combustor wall heat flux values of 0.23 and 1.63 Btu/s-in^2 (38 and 266 W/cm^2, respectively) for vehicles traveling at freestream Mach numbers of 6 and 10, respectively. The associated combustor adiabatic wall temperatures for these notional Mach 6 and Mach 10 aircraft combustors are 1390 and 3060°C, respectively. These wall temperatures are unsustainable by conventional materials and therefore require novel cooling schemes, e.g., regenerative cooling.

In order to limit the deleterious fouling reactions under these severe temperatures and flux conditions, jet fuel requires limited exposure time, e.g., milliseconds. These high wetted wall temperatures and short fuel residence times impose large thermal gradients on the fuel. The effects of such large thermal gradients and high heat fluxes on jet fuel thermal stability has gone largely unreported in the literature. However, studies of jet fuel fluid dynamics and heat transfer under these high heat flux conditions (Hitch & Karpuk, 1997; Hitch & Karpuk, 1998; Linne et al., 2000). Hitch & Karpuk (1997; 1998) reported the occurrence of Helmholtz flow oscillations which were characterized by pressure fluctuations of about ±50 to 60 psi, occurring at frequency ranges of 1-2 Hz and 75-450 Hz, causing complete reversal of the fluid flow direction. Linne et al. (2000) reported even more severe pressure fluctuations of up to 1000 psi at a frequency of about 1900 Hz. Both groups used JP-7 in their studies and operated above the critical pressure, with reported surface temperatures above the critical temperature. Under some conditions these groups also reported deviations of the heat transfer coefficient from typical behavior.

The observance of heat transfer deterioration (HTD) and heat transfer enhancement have been well reported in the literature for other supercritical fluid systems (Yamagata et al., 1972; Song et al., 2008; Hua et al., 2010; Pizzarelli et al., 2010). The occurrence of HTD is attributed to the presence of large heat fluxes relative to the corresponding mass fluxes within the heat transfer tubes. However, explanation of HTD phenomenon in forced convective flows has been somewhat varied including: analogies to film boiling and the presence of an insulating supercritical film which inhibits heat transfer, and a reduction in turbulent diffusion due to a characteristic “M-shaped” velocity profile.

Nevertheless, HTD and oscillatory flow instabilities can lead to rapid component failure due to reduced heat transfer and an increase in thermal fatigue.

Computational modeling of fluid dynamics and thermodynamics of fuel systems has become routine over the past decade with the advent of robust commercial CFD software and inexpensive computational power. However, it is still incumbent upon the CFD analyst to determine the appropriate form of the conservation equations to be solved. Turbulence models, especially, require careful selection as many different schemes are available such as, but not limited to: Reynolds-averaged Navier-Stokes (RANS), large eddy simulation (LES), and detached eddy simulation (DES) (ANSYS, 2010b). There are many RANS-based turbulence models – one of the most common turbulence modeling schemes – all of which are based on decomposing the instantaneous Navier-Stokes equations into a time averaged and a fluctuating component such that:

$$\phi = \overline{\phi} + \phi'$$

where ϕ represents any scalar quantity, e.g., pressure, energy, velocity, or species concentration, $\overline{\phi}$ represents the mean or time averaged scalar component, and ϕ' represents the fluctuating scalar component. The momentum equation may then be written, in Cartesian form, as follows:

$$\frac{\partial}{\partial t}(\rho\overline{u}_i) + \frac{\partial}{\partial x_j}\left(\rho\overline{u}_i\overline{u}_j\right) = -\frac{\partial p}{\partial x_j} + \frac{\partial}{\partial x_j}\left[\mu\left(\frac{\partial\overline{u}_i}{\partial x_j} + \frac{\partial\overline{u}_j}{\partial x_i} - \frac{2}{3}\delta_{ij}\frac{\partial\overline{u}_l}{\partial x_l}\right)\right] + \frac{\partial}{\partial x_j}\left(-\rho\overline{u'_i u'_j}\right)$$

where ρ is density, $\overline{u}$ is the mean velocity, δ_{ij} is the Kronecker delta, and the $-\rho\overline{u'_i u'_j}$ term represents the Reynolds stresses. This Reynolds stress term must be modeled in order to close the momentum equations, which is where the individual RANS-based turbulence models differ in their approach.

Previous works, involving the modeling of jet fuel systems, have successfully used the two-equation, standard κ-ε turbulence model to close the momentum equations (Katta & Roquemore, 1993; Ervin et al., 1996). The standard κ-ε model does not completely resolve the viscous boundary layer, instead a semi-empirical "wall function" is used to approximate the near wall zone. Recently, Jiang (2011) showed that the standard κ-ε model was inadequate at predicting heat transfer to jet fuel under conditions of high heat flux, because the lack of near wall resolution led to improper prediction of the heat transfer characteristics. RANS-based turbulence models with better near-wall resolution, such as κ-ε models with enhanced wall treatment (EWT) or κ-ω models, should provide better accuracy for cases where viscous sub-layer resolution is required. EWT of the ε-equation, in κ-ε models, divides the flow domain into two zones: a viscosity affected region and a fully-turbulent region, whose delineation is based on a wall-distance function. The κ-ω models can be integrated through the viscous sub-layer, and therefore, provide intrinsic resolution of the viscous sub-layer; however, solutions of the standard κ-ω model tends to be sensitive to the inlet free-stream turbulence properties (ANSYS, 2010b). The shear-stress transport (SST) κ-ω model, developed by Menter (1994), uses the κ-ω model near the wall and the κ-ε model in the bulk flow, thus taking advantage of the strong points of both turbulence models. Blending functions are used to transition between the near wall and the free-stream flow regions, which makes the SST κ-ω turbulence model an overall robust method for most flows (ANSYS, 2010b).

Research Objectives

The previous discussion has demonstrated that the chemistry of jet fuel autoxidation is complex and incomplete. Additionally, there is a need for robust chemical and physical models for conditions of high flux heat transfer. Therefore, the aim of this work is twofold: measure the kinetic parameters of hydroperoxide decomposition relevant to jet fuel, and determine if a pseudo-detailed chemical kinetic mechanism with CFD can be extended to study the complex behavior of jet fuel under conditions of high flux heat transfer.

The following chapter of this work (Chapter II) will address the experimental and numerical procedures that were used to generate the data reported in subsequent chapters. Chapter III explores the kinetics of some fundamental hydroperoxide decomposition pathways pertinent to jet fuel thermal stability. The pathways that will be explored in Chapter III include: simple thermal homolysis; dissolved metal assisted, weak acid assisted, and a combination of dissolved metal and weak acid assisted hydroperoxide decomposition, and the mitigating effects of MDA. Experimental conditions have been chosen to relate closely to that of real jet fuel thermal stress conditions, i.e., hydrocarbon solvent, 100 to 200°C, hydroperoxide concentration of $\leq$1.8 mM, TAN $\leq$0.015 mg KOH/g, and dissolved metal levels in the ppb to low ppm range. Also, the role of hydroperoxide decomposition reactions on jet fuel surface deposition will be explored via experimental measurement of deposition during hydroperoxide decomposition in jet fuel in the absence of competing autoxidation reactions.

In Chapter IV, the kinetic parameters of hydroperoxide decomposition will be applied to a pseudo-detailed chemical kinetic model and used with CFD to predict conditions of jet fuel high flux heat transfer. Experimental data from laminar flow and transitional flow heat transfer studies will be used to validate CFD models. The corresponding chemical mechanism predictions will be compared to experimental oxygen and carbon deposition data to determine if this chemical mechanism can be extended to such severe conditions. Finally, Chapter V will provide a summary and recommendations for future studies.

CHAPTER II

EXPERIMENTAL & NUMERICAL PROCEDURES

Introduction

The experimental and numerical procedures used to determine the catalytic effects on hydroperoxide decomposition (Chapter III) and the effects of high flux heat transfer on jet fuel (Chapter IV) will now be presented. The first three sections of this chapter address the experimental procedures used to determine the reaction rates and Arrhenius parameters for hydroperoxide decomposition in Chapter III. The fourth section of this chapter gives detailed information about the reagents used for the experiments reported in both Chapter III and IV. Finally, the last two sections of this chapter address the experimental and numerical procedures, respectively, used for the high flux heat transfer experiments reported in Chapter IV.

Hydroperoxide Decomposition Procedure

A 316 stainless steel Parr reaction vessel, about 100 mL total volume, equipped with a thermocouple, pressure transducer, headspace dissolved oxygen sensor, and syringe sampling port was used to conduct all of the kinetic experiments. The reaction liquid was well stirred using a magnetic stir bar. The experiments were conducted by first loading the reaction vessel with 60 mL of surrogate fuel, i.e., Exxsol D-80. Exxsol D-80 is an aliphatic hydrocarbon distillate within the jet fuel range which contains very low heteroatom levels. A low flow (≤ 20 mL/min) of dry nitrogen gas was bubbled through the surrogate fuel for at least one hour to remove oxygen from the system, which was verified by oxygen sensor readings. Once purged of oxygen, the reactor was then closed and heated to the desired reaction temperature in the range of 105 to 205°C. After reaching the proper temperature, hydroperoxide reagent was injected via the syringe port and allowed to mix for one minute. Sample aliquots of about 1 to 2 mL were then pulled via the syringe port at regular intervals for subsequent hydroperoxide analysis. The hydroperoxide quantitative analysis was conducted via a previously reported triphenylphosphine (TPP) method, where the TPP reacts quantitatively with the hydroperoxides in a sample to produce triphenylphosphine oxide (TPPO) with subsequent GC-FID detection of the TPPO (West et al., 2005). Organometallics, naphthenic acids, and metal deactivator additive were added to the surrogate fuel prior to oxygen removal and heating. Replicate runs were conducted for some rate experiments and the relative standard deviation (RSD) was computed for these rate constants, k. Also, the 95% confidence interval was computed for Arrhenius parameters, E_a and A, when rate data was collected at more than three temperatures.

Hydroperoxide Production Procedure

Dodecane hydroperoxide (DHP) and ethylbenzene hydroperoxide (EBHP) solutions, which were not available commercially, were generated by low temperature oxidations of n-dodecane and ethylbenzene, respectively, with an overpressure of air. The n-dodecane low temperature oxidation was carried out by charging the Parr reactor with 60 mL of solvent and 95 psia of air, and then heating the reactor to 100°C for 97 hours. The ethylbenzene low temperature oxidation was carried out by charging the reactor with 60 mL of solvent and 73 psia of air, and then heating the reactor to 80°C for 96 hours. After the reaction period, both the DHP and EBHP reagent mixtures were allowed to cool to room temperature and then analyzed for hydroperoxide content. The DHP and EBHP reagent concentrations were verified to be 19.5 mM and 81.8 mM, respectively. The hydroperoxide reagents were kept in refrigerated storage until use.

Quartz Crystal Microbalance (QCM) Deposition Measurements

The QCM system (Figure 4) has been described in detail previously (Klavetter et al., 1993; Zabarnick, 1994; Zabarnick & Grinstead, 1994). A jet fuel sample, 60 mL, was heated in the QCM system to 140°C in the absence of oxygen to limit autoxidation reactions. After reaching temperature, cumene hydroperoxide (CHP) was added to the fuel via syringe to a concentration of 16 mM. Deposition was followed in time via monitoring of the QCM frequency using the following equation (Klavetter et al., 1993):

$$\rho_s = -2.21 \times 10^5 \cdot \left(\frac{f - f_o}{f_o^2}\right)$$

Where ρ_s is the deposit surface mass density with units of μg/cm^2, f_o is the initial crystal resonant frequency in MHz, and f is the crystal frequency in MHz. Deposition measurements versus time were recorded to observe the effect of added copper naphthenates, naphthenic acids, metal deactivator and their combinations.

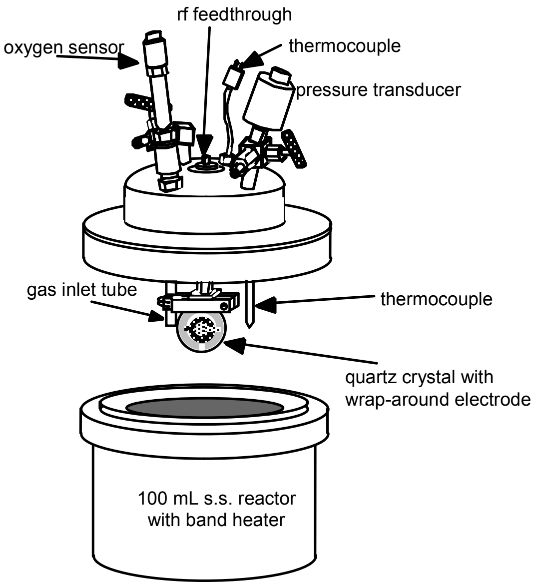

Figure 4. Diagram of the QCM apparatus (Mick, 1998).

Reagents

Exxsol D-80 (dearomatized aliphatic hydrocarbon) was obtained from ExxonMobil Corp. and used without further purification. Specification *JP-8 jet fuel* (reference number POSF-4751) was obtained from the Wright-Patterson Air Force Base flight line and used as received (Table 2). The following chemicals were also used as received: *Cumene hydroperoxide* (CHP), 88%, Sigma-Aldrich; *n-Dodecane*, anhydrous, 99+%, Sigma-Aldrich; *Ethylbenzene*, anhydrous, 99.8+%, Sigma-Aldrich; *Copper naphthenates* (Cu-na), tech grade, Sigma-Aldrich; *Iron Naphthenates* (Fe-na), 12 %wt Fe, *Manganese Naphthenates* (Mn-na), 6 %wt Mn, *Zinc Naphthenates* (Zn-na), 10 %wt Zn, Strem Chemicals, Inc.; *Copper bis(2,2,6,6-tetramethyl-3,5-heptanedioate)* (Cu-tmhd), 99%, Acros Organics; *Naphthenic acids* (NA), pract., 230-260 mg KOH/g, Acros Organics; *N,N'-Bis(salicylidene)-1,2-propanediamine* (Metal Deactivator Additive [MDA]), CAS No. 94-91-7, 98%, TCI America.

Table 2. Selected Specification Results for JP-8 Jet Fuel (POSF-4751)

Method	Test	Result
ASTM D2622	Sulfur (ppm wt)	427
ASTM D3242	Total Acid Number (mg/KOH/g)	0.003
ASTM D1319	Aromatics (% vol)	19.6
ASTM D3227	Mercaptan Sulfur (% mass)	0.000
ASTM D1840	Naphthalenes (% vol)	1.0
ASTM D3241	Thermal Stability @ 260°C	
	Change in Pressure (mmHg)	0
	Tube Deposit Rating, Visual	1

High Heat Flux Apparatus

The experimental apparatus used to thermally stress jet fuel has been described in detail elsewhere (Jiang, 2011). The apparatus, shown in Figure 5, primarily consists of a vertically oriented 316 stainless steel tube (test specimen) which is heated by passing current through the tube wall via a 50 kVA DC power supply. Vertical upward fuel flow is used to minimize buoyancy effects experienced during horizontal flow (Katta et al., 1995). Temperature, pressure, flow rate, and dissolved oxygen measurements are monitored and recorded at various locations throughout the apparatus. Experiments were conducted by increasing the electrical power to the test specimen until the desired bulk fuel outlet temperature was reached. The power was adjusted to keep the target outlet temperature for the duration of the run (25 min). The total power supplied to the test specimen was limited by the maximum safe use temperature of the tube (~800°C) which was monitored by K-type thermocouples strap-welded at fixed intervals to the outer wall of the heated section of the test specimen. Table 3 lists the test specimen geometries and operating parameters for the two experimental runs that will be discussed. The heated length of the tube is the section actively heated by electrical resistance; however, the total length includes an extra 6 inches of tubing (exit region) after the heated zone that is not actively heated before the point at which the outlet (bulk) fuel temperature is measured. All bulk fuel conditions, e.g., temperature, dissolved oxygen, and Reynolds number (Re), are reported at the exit of the total test specimen length, not the heated length, unless otherwise specified.

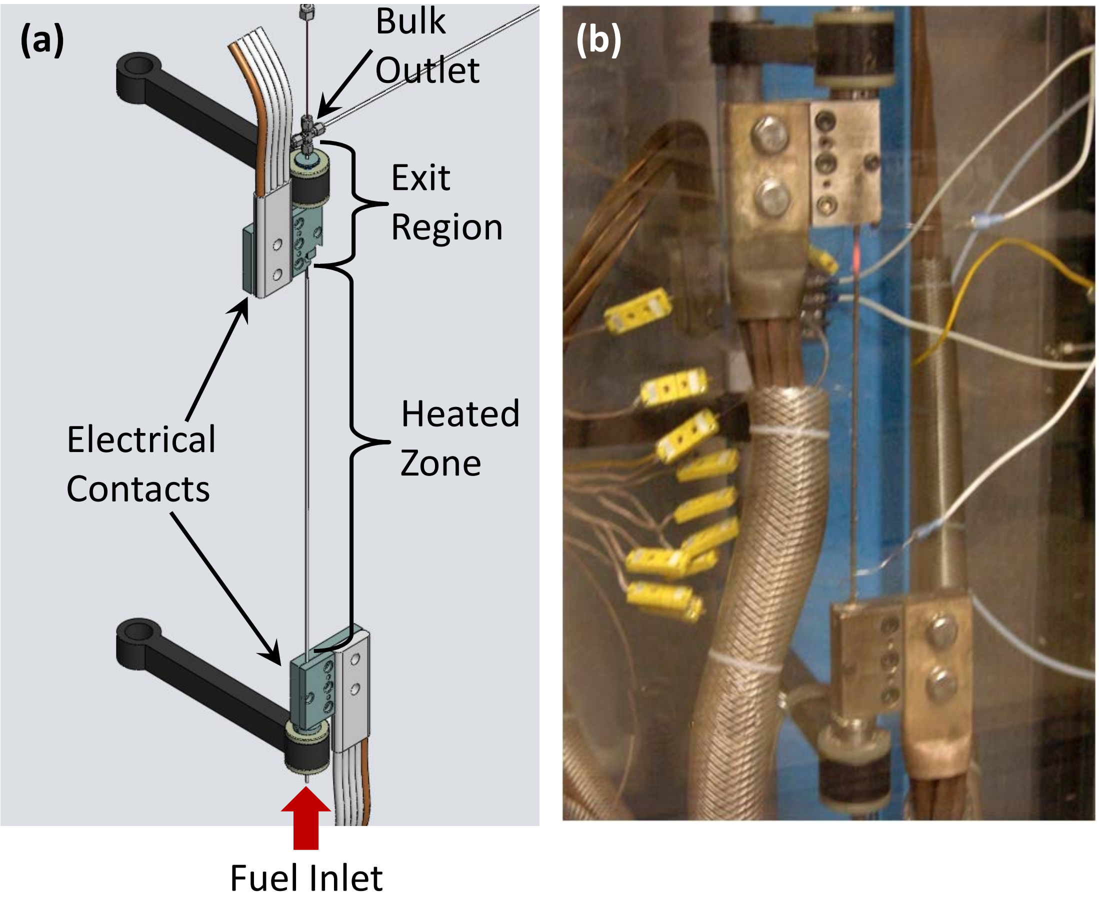

Figure 5. Jet fuel high heat flux thermal stability apparatus (a) diagram, and (b) photograph showing portion of tube visibly red-hot.

Table 3. Test Specimen Dimensions and Experimental Operating Conditions

Parameter	Case A	Case B
Material Type	316 Stainless Steel	
Heated Length [Total Length] (in)	5 [11]	10 [16]
Outer Diameter (in)	0.125	
Inner Diameter (in)	0.085	
Inlet Flow Rate (mL/min)	300	
Inlet Fuel Temperature (°C)	25	
Power Input (Btu/s)	0.35	1.3
Uniform Heat Flux (Btu/s-in^2)	0.26	0.49
Inlet Reynolds Number	1,600	1,700
Outlet Reynolds Number	2,500	5,900
Pressure (psia)	800	
Duration (min)	25	
Fuel Residence Time (ms)	~90	~180

Numerical Simulations

Computational simulations were performed using the commercially available CFD software: ANSYS Fluent®, version 13 (ANSYS, 2010a). The Fluent software solves a finite volume set of the mass, species transport, energy, and momentum conservation equations (Navier-Stokes equations) (Appendix A). Also, closed forms of the turbulent kinetic energy, κ, and the specific dissipation rate, ω, transport equations were solved when turbulent flow was modeled. Simulations were carried out in double precision mode using the SIMPLEC pressure based solver with a skewness correction factor of 1. The least squares cell based discretization scheme was used for gradients, the standard discretization scheme was used for pressure, and a second order upwind scheme was used for all other quantities. The flow system modeled was assumed to be steady state and axisymmetric. A gravitational force term of 9.8066 m/s^2 was included in the direction opposite of flow (negative axial direction).

Two methods of representing the physical boundary conditions for the energy equation were used in this study and are shown schematically in Figure 6. Both methods have a uniform volumetric source term, q''', in the heated zone of the tubing, adiabatic outer walls in the non-heated tubing zones, and coupled heat transfer of the liquid-solid surfaces. The first method (Scheme 1) assumes a mixed convection-radiation outer wall boundary condition in the heated zone, based on typical quiescent air and surrounding property conditions as follows: 27°C ambient temperature, an emissivity of 1.0, and a heat transfer coefficient of 25 W/m^2-K to the surrounding static air. The second method (Scheme 2) assumes a constant outer wall temperature profile, which was generated using a best fit function of the experimental thermocouple measurements. The q''' was determined by dividing the estimated power input, $\dot{q}$, by the volume of metal in the heated zone such that:

$$\dot{q} = \dot{m}(H_{outlet} - H_{inlet})$$

$$q''' = \frac{\dot{q}}{\pi(r_{outer}^2 - r_{inner}^2)l}$$

Where $\dot{m}$ is the total inlet mass flow rate, H_{inlet} & H_{outlet} are the specific enthalpies of the fuel at the heated zone inlet and exit region outlet, respectively, r_{inner} & r_{outler} are the inner and outer tube radii, respectively, and l is the heated zone length. Enthalpies were derived from thermocouple data of the bulk fluid at the inlet and outlet locations.

Physical properties of jet fuel were estimated using NIST SuperTrapp software, version 3.0, which uses the Peng-Robinson equation-of-state correlation (Huber, 1999). The NIST SuperTrapp software is able to estimate properties of petroleum fractions using the API gravity and average boiling point as inputs to define the distillate fraction. The JP-8 jet fuel used in this study had a measured API gravity of 42.3 and an average boiling point of 207°C. Tabulated property data for density, constant pressure heat capacity, thermal conductivity, and viscosity, at 800 psia, was exported as a function of temperature and used for numerical computations (Appendix B).

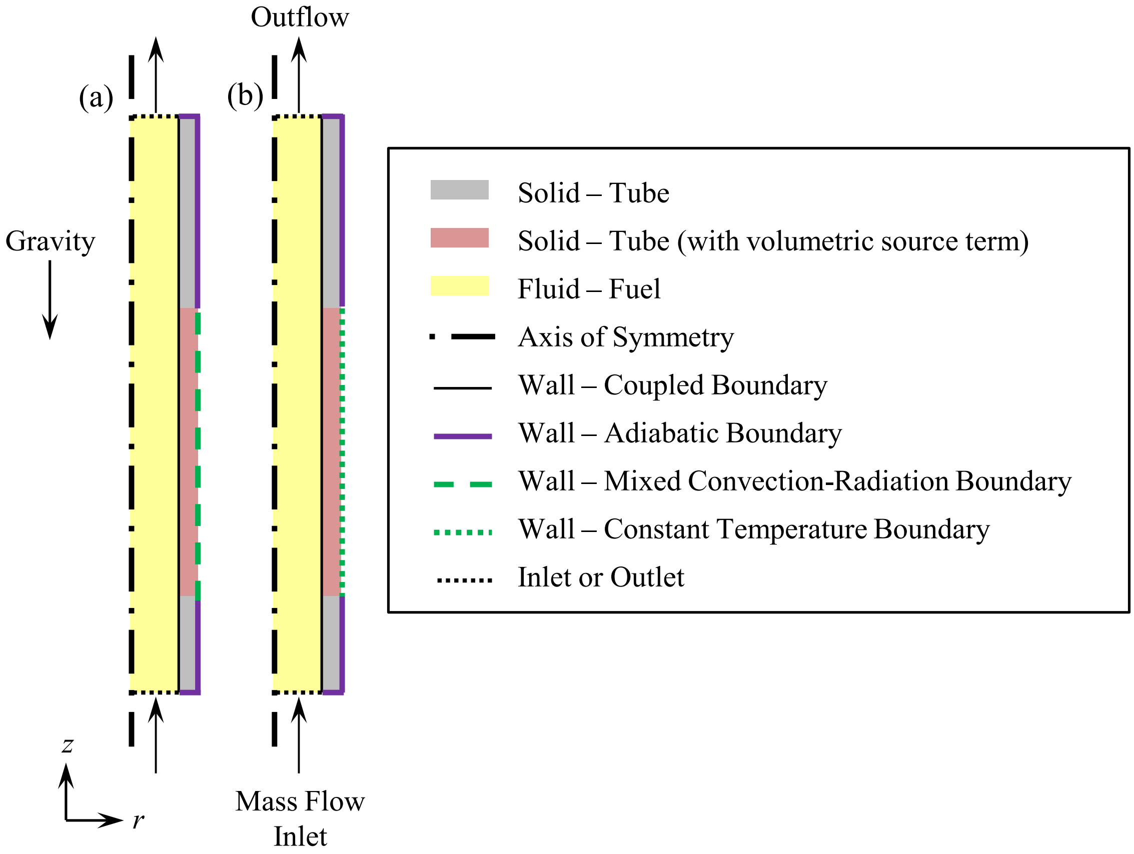

Figure 6. Depiction of numerical boundary conditions (a) Scheme 1 and (b) Scheme 2.

Jet fuel autoxidation and deposition kinetics were modeled using the pseudo-detailed chemical kinetic model listed in Table 5. Volumetric and wall surface reactions – with mass deposition source – were enabled in Fluent. The laminar finite-rate model was used for the turbulence-chemistry interaction. A constant mass diffusion term of 8×10^{-8} m/s^2 was used for all species. The inlet species mass fractions used in the model are listed in Table 4 and are based on measurements of the JP-8 jet fuel reported above. All other species inlet amounts in the model were set equal to zero except RH which comprised the balance.

Table 4. Inlet Species Mass Fractions

Species	Inlet Mass Fraction
AH	5.9×10^{-5}
SH	6.7×10^{-4}
O_2	7.1×10^{-5}
M	6.8×10^{-8}
RO_2H	5.2×10^{-6}

Table 5. Pseudo-Detailed Chemical Mechanism for Autoxidation of Jet Fuel (Kuprowicz et al., 2007)

No.	Reaction	Arrhenius Factor (mol, L, s)	E_a (kcal/mol)
1	$R\cdot + O_2 \rightarrow RO_2\cdot$	3.0×10^9	0
2	$RO_2\cdot \rightarrow R\cdot + O_2$	1.0×10^{14}	15
3	$RO_2\cdot + RH \rightarrow RO_2H + R\cdot$	3.0×10^9	12
4	$RO_2\cdot + RO_2\cdot \rightarrow ROH + \text{Aldehyde} + O_2$	3.0×10^9	0
5	$RO_2\cdot + AH \rightarrow RO_2H + A\cdot$	3.0×10^9	5
6	$A\cdot + RH \rightarrow AH + R\cdot$	1.0×10^5	12
7	$A\cdot + RO_2\cdot \rightarrow \text{Products}_{AH}$	3.0×10^9	0
8	$RO_2H \rightarrow RO\cdot + \cdot OH$	2.0×10^8	25
9	$RO_2H + M \rightarrow RO\cdot + \cdot OH + M$	1.0×10^9	12
10	$RO\cdot + RH \rightarrow ROH + R\cdot$	3.0×10^9	10
11	$RO\cdot \rightarrow R'\cdot + \text{Carbonyl}$	1.0×10^{16}	15
12	$\cdot OH + RH \rightarrow H_2O + R\cdot$	3.0×10^9	10
13	$R'\cdot + RH \rightarrow \text{Alkane} + R\cdot$	3.0×10^9	10
14	$RO_2H + SH \rightarrow \text{Products}_{SH}$	3.0×10^9	18
15	$RO_2\cdot + R\cdot \rightarrow RO_2R$	3.0×10^9	0
16	$R\cdot + R\cdot \rightarrow R_2$	3.0×10^9	0
17	$R\cdot + O_2 \rightarrow \text{Olefin} + HO_2\cdot$	3.0×10^9	5
18	$HO_2\cdot + RH \rightarrow H_2O_2 + R\cdot$	3.0×10^9	10
19	$HO_2\cdot + HO_2\cdot \rightarrow H_2O_2 + O_2$	3.0×10^9	0
20	$RO_2\cdot + HO_2\cdot \rightarrow RO_2H + O_2$	3.0×10^9	0
21	$\text{Products}_{AH} \rightarrow \text{Solubles}_{AH}$	1.0×10^9	0
22	$\text{Products}_{AH} \rightarrow \text{Insolubles}_{AH}$	3.8×10^{10}	6.5
23	$\text{Insolubles}_{AH} \rightarrow \text{Surface Deposits}_{AH}$	3.0×10^3	16.3
24	$\text{Products}_{SH} \rightarrow \text{Solubles}_{SH}$	1.0×10^9	0
25	$\text{Products}_{SH} \rightarrow \text{Insolubles}_{SH}$	3.8×10^{10}	6.5
26	$\text{Insolubles}_{SH} \rightarrow \text{Surface Deposits}_{SH}$	3.0×10^3	16.3
27	$RH \rightarrow R'\cdot + R'\cdot$	1.0×10^{16}	65

Grid independence studies were conducted by first varying the number of radial cells, while keeping the number of axial cells constant, and monitoring the bulk outlet temperature and oxygen mass fraction. Then, the axial cell number was varied while keeping the radial number of cells constant. Table 6 lists the conditions for the Case B grid independence study. The data shows that Case B was found to be grid independent with 10,640 cells (11,281 nodes) with: 5 evenly spaced radial cells (0.004 in) and 304 evenly spaced axial cells (0.0625 in) in the solid tube wall, and 30 biased radial cells (1:1000 bias with smallest cell near the wall) and 304 evenly spaced axial cells (0.0625 in) in the fluid. A representation of the mesh is shown in Figure 7. Similarly, Case A was found to be independent of the mesh for a grid size of 5,600 cells with: 5 evenly spaced radial cells (0.004 in) and 224 evenly spaced axial cells (0.0625 in) in the solid tube wall, and 20 biased radial cells (1:1000 bias) and 224 evenly spaced axial cells (0.0625 in) in the fluid. An extra 3 inch length of tube was added to the inlet side of each computational case as an entrance region prior to the heated length. While this extra section of tubing was included in the grid study, and subsequent computations, the results from this extra portion of tubing were not reported as this entrance portion had little consequence on the results of interest.

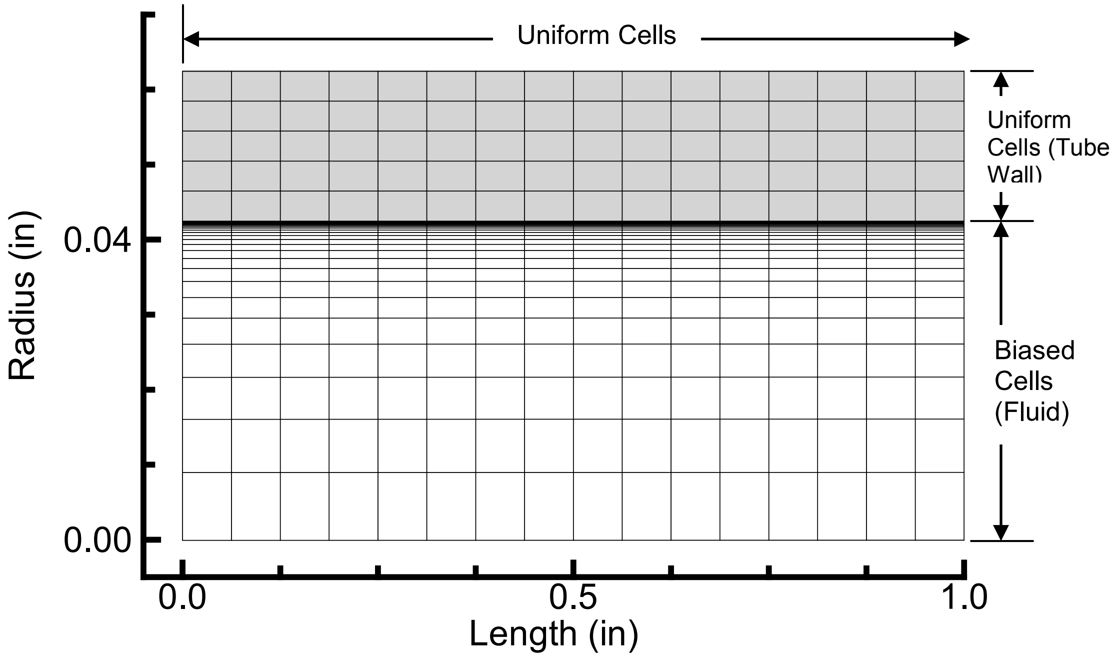

Figure 7. Representative portion of the axisymmetric mesh used for numerical simulations.

Table 6. Case B Grid Independence Data

Axial Cell Size (in)	Radial Cell Number	Nodes	Outlet Temperature (°C)	Outlet O_2 Mass Fraction ($\times 10^{-5}$)
0.125	25	4,892	445	6.59
0.125	30	5,657	455	6.61
0.125	35	6,422	457	6.61
0.125	30	5,657	455	6.61
0.0625	30	11,281	441	6.59
0.03125	30	22,529	441	6.58

CHAPTER III

CATALYTIC DECOMPOSITION OF HYDROPEROXIDES

Introduction

Hydroperoxides are a critical intermediate species in jet fuel chemistry. The homolytic decomposition of hydroperoxides accelerates the free radical autoxidation chain mechanism, while reactions with reactive sulfur species create deposit precursors. Chemical species that accelerate hydroperoxide decomposition pathways, e.g., metals and carboxylic acids, can pose a risk to jet fuel thermal stability. This chapter examines jet fuel-relevant pathways for catalytic decomposition of hydroperoxides and presents data that can be used for chemical kinetic modeling. Data will also be presented to show how hydroperoxide interactions with these catalytic agents can affect deposition.

Unassisted Hydroperoxide Decomposition

Arrhenius parameters for the homolytic decomposition of fuel hydroperoxides must be established as a basis before examining catalytic effects. However, before these homolytic Arrhenius parameters could be measured, experiments were performed to verify the reaction order and that secondary reactions were minimized. Cumene hydroperoxide (CHP) was thermally decomposed at 165°C with three initial CHP concentrations of about 1.6, 1.1, and 0.55 mM in Exxsol D-80. Exxsol D-80 was selected as a suitable jet fuel surrogate as it is a commercially available, aliphatic solvent that has a very low heteroatomic level and is within the jet fuel distillate range. To completely isolate the hydroperoxide decomposition reaction from interfering autoxidation reactions, the reaction vessel and liquid sample were first sparged with nitrogen to completely remove all oxygen from the system. Figure 8 shows the results of the CHP decomposition experiment, plotting the logarithm of the CHP concentration versus time. As the figure shows, the three sets of data can be fit with similar slopes, i.e., all three fits have a slope within 4% relative to one another and R^2 values of ≥ 0.991. These linear fits, over a range of initial RO_2H concentrations, show that the decomposition of CHP is in accord with a unimolecular first order process over the concentration range of interest, with no evidence of interference from secondary reactions.

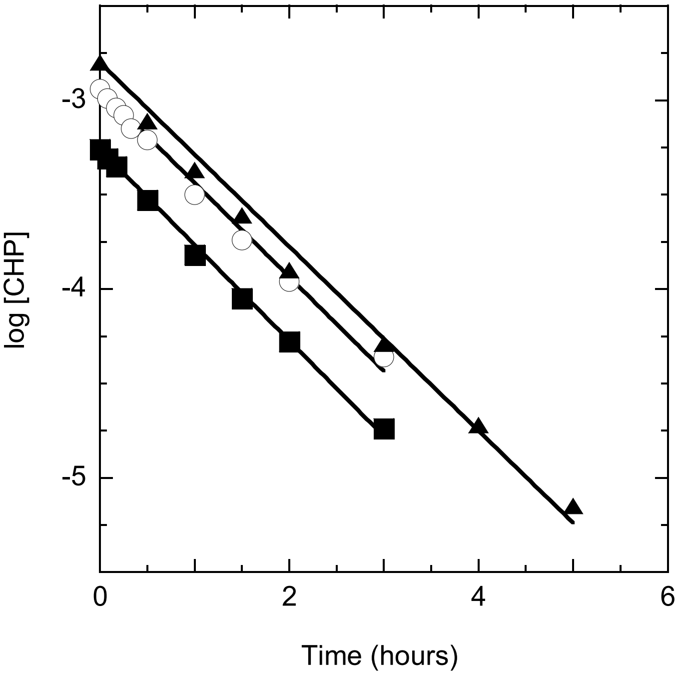

Figure 8. Decomposition of CHP in Exxsol D-80 at 165°C with initial CHP concentrations of: (■) 0.55 mM, (○) 1.1 mM, and (▲) 1.6 mM.

It has been shown that the unimolecular first order decomposition rate of hydroperoxides can be measured in the liquid phase; therefore, some additional fuel hydroperoxides, dodecane hydroperoxide (DHP) and ethylbenzene hydroperoxide (EBHP), will be examined to determine their relative reactivity. CHP, DHP, and EBHP were thermally decomposed, separately, in Exxsol D-80 at 145°C with an initial hydroperoxide level of about 0.5 mM. Again, oxygen was removed from the system to prevent interfering autoxidation reactions and the hydroperoxide concentrations were monitored over time. Figure 9 shows the resulting logarithm of the normalized hydroperoxide concentrations, i.e., hydroperoxide concentration divided by the initial hydroperoxide concentration, versus time. As the figure shows, the three sets of hydroperoxide data are linear, thus all three hydroperoxide decompositions fit first order behavior at this temperature. There is also a significant difference in the decomposition rates of the three hydroperoxides where the decomposition rates follow the order: EBHP > DHP > CHP. Researchers have often assumed that unimolecular hydroperoxide decomposition rates are independent of the hydroperoxide R group (Benson, 1981). However, recent calculations show the O-O bond strength can vary with the R group, especially for vinyl hydroperoxides which exhibit very weak O-O bond strengths (Sebbar et al., 2002).

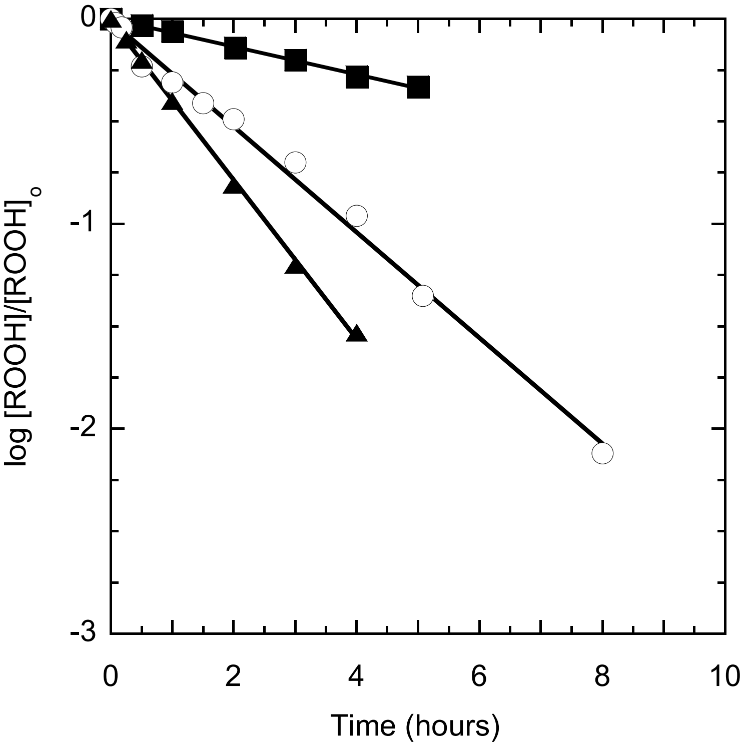

Figure 9. First order decomposition of: (■) CHP, (○) DHP, and (▲) EBHP at 145°C.

For development of improved chemical kinetic mechanisms, it is desirable to obtain Arrhenius parameters for the unimolecular, thermal decomposition of hydroperoxides in the liquid phase under representative jet fuel conditions. Thus CHP decomposition rate experiments were conducted at seven temperatures from 105 to 205°C, with the results shown in Figure 10 and the calculated Arrhenius parameters listed in Table 7. The CHP thermal decomposition data in Table 7 are in good agreement with literature values (Nurullina et al., 2006), as discussed later, which gives confidence in the current experimental procedure. Arrhenius parameters were also determined for DHP and EBHP over a limited temperature range using only three temperatures, with the experimental results shown in Figure 10 and listed in Table 7. The Arrhenius parameters for DHP and EBHP are not significantly different from those of CHP even though the individual rate constant data are significantly different (Figure 9) for the three hydroperoxides, this discrepancy is probably due to the limited number of temperatures for which data was collected for DHP and EBHP.

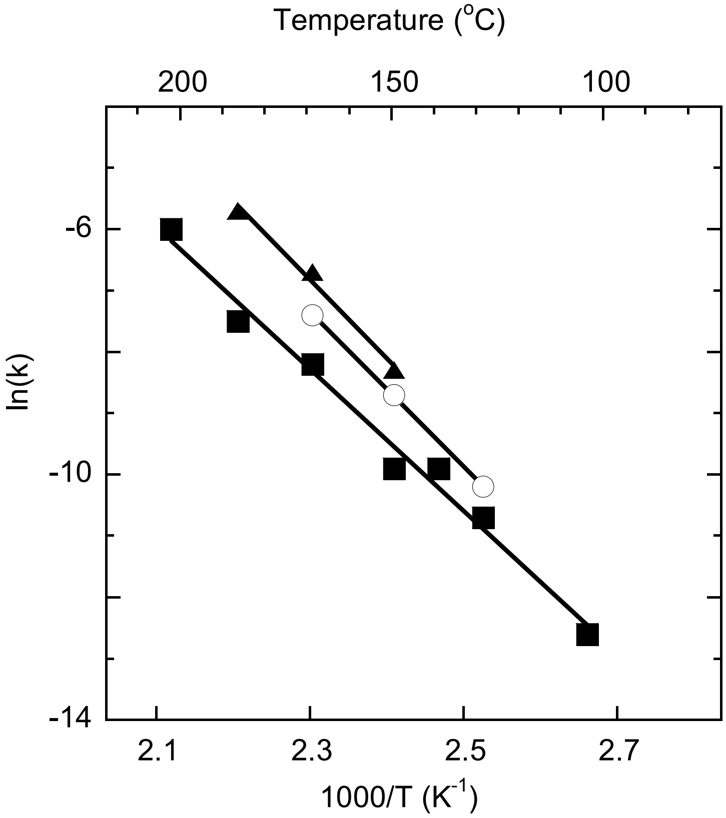

Figure 10. Arrhenius plot of the first-order, liquid phase decomposition of: (■) CHP, (○) DHP, and (▲) EBHP.

Table 7. Arrhenius Parameters for First-Order, Liquid Phase Hydroperoxide Decompositions

Hydroperoxide	E_a (kcal/mol)	Log(A) (s^{-1})	No. of Exp. Temps.
CHP	23 ±3	7.6 ±1.5	7
DHP	24	9.0	3
EBHP	25	9.4	3

Assisted Hydroperoxide Decomposition

With the unimolecular decomposition order and Arrhenius parameters obtained for CHP thermal decomposition, experiments were conducted to determine the effect of dissolved metals on these measured rates. Metals were dissolved in Exxsol D-80 using various metal naphthenates at 0.012 to 0.015 mM of metal (~1 ppm by weight of metal) prior to oxygen removal, heating, and CHP introduction. The experiments were carried out at a range of temperatures from 105 to 205°C with an initial CHP concentration of about 0.5 mM. The measured pseudo-first order rate constants, k, of CHP decomposition are listed in Table 8. Also listed in the table for the metal containing experiments is the relative rate constant, k/k_o, that is the pseudo-first order rate constant of CHP decomposition with metal divided by the rate constant without metal, k_o. The data shows that the addition of metal naphthenate increases the relative decomposition rate of CHP, i.e., $k/k_o \geq 1$, in all experimental cases except one: the addition of zinc naphthenate (Zn-na) at 125°C. Very large increases in k/k_o were noticed for experiments involving copper naphthenate (Cu-na) and manganese naphthenate (Mn-na) at temperatures of 145°C and lower. The decomposition of CHP proceeded so rapidly with the addition of Mn-na that it became impractical to measure rate data at temperatures of 165°C and greater. While the addition of copper increased k/k_o under all experimental circumstances, there was a marked difference in activity between the two copper species examined. The addition of Cu-na increased k/k_o much more than Cu-tmhd, even though the two species were added with equal levels of copper.

Table 8. Rate Constants for Liquid Phase CHP Decomposition

T (°C)	Metal Species	k (10^{-6}/s)	%RSD[a]	k/k_o
105	-	3.5		-
	Cu-na	110		31
	Cu-tmhd	29		8
	Mn-na	1,500		429
125	-	22		-
	Cu-na	200		9
	Cu-tmhd	50		2
	Fe-na	69		3
	Mn-na	1,900		86
	Zn-na	18		0.8
135	-	51	23 (2)	-
	Cu-na	380		7
145	-	48	15 (2)	-
	Cu-na	490		10
	Cu-tmhd	160		3
	Fe-na	310		6
	Mn-na	6,200		129
165	-	280	27 (4)	-
	Cu-na	750	9 (3)	3
	Cu-tmhd	950		3
	Fe-na	1,000		4
	Zn-na	353		1.3
185	-	540		-
	Cu-na	1,900		4
	Cu-tmhd	2,800		5
205	-	2,600		-
	Cu-na	5,800		2

[a] Values in parentheses are the number of replicate runs used to compute the % RSD.

The rate data from Table 8 was used to generate Arrhenius parameters, listed in Table 9, for the pseudo-first order decomposition of CHP with dissolved metal naphthenates. As the data shows, iron and zinc do not cause a significant change in the activation energy of CHP decomposition under these experimental conditions. Conversely, copper and manganese both significantly decrease the pseudo-first order activation energy and A-factor for unimolecular hydroperoxide decomposition. These results indicate that the decomposition of CHP proceeds via lower energy reaction pathways when Cu-na or Mn-na is present.

Table 9. Arrhenius Parameters for Pseudo-First Order, Liquid Phase Decomposition of CHP with 1 ppm Dissolved Metal Naphthenates

Metal Naphthenate	E_a (kcal/mol)	Log(A) (s^{-1})	No. of Exp. Temps.
Fe	23	8.6	3
Zn	26	9.4	2
Cu	14 ±3	3.8 ±1.5	8
Mn	11	3.4	3

With the effect of various dissolved metals on the decomposition of CHP determined, it is now desirable to examine the consequence of dissolved acids on the CHP decomposition rate. Experiments were conducted by dissolving naphthenic acids (NA) in Exxsol D-80 to a level of 0.128 mM KOH (0.009 mg KOH/g) prior to oxygen removal, heating, and CHP introduction. Commercially available NA, which is a petroleum derived mixture of cycloparaffinic carboxylic acids, was selected because according to the CRC (2004) NA are believed to be relevant jet fuel acids. As was done previously, the CHP concentration was monitored over time and the resulting pseudo-first order rate constants are listed in Table 10 for four different temperatures. As the data show, the addition of NA increases the decomposition rate of CHP for three out of the four temperatures examined. However, the maximum observed increase in k/ko for NA was much less than that observed for the metal naphthenates even though the NA was present at about 10 times the concentration of the metal; therefore, the metal naphthenates had a much greater effect on hydroperoxide decomposition than NA.

Table 10. Rate Constants of Liquid Phase CHP Decomposition with 0.128 mM Naphthenic Acids

T (°C)	k (10^{-6}/s)	k/k_o
105	9.2	2.6
125	16	0.7
145	90	1.9
165	430	1.5

It has been shown that reactive metal species such as Cu-na can dramatically increase the rate of hydroperoxide decomposition at low temperatures, ≤145°C. Conversely, less reactive metal species such as Zn-na and moderately reactive naphthenic acids have shown, at most, a modest increase in the hydroperoxide decomposition rate. However, acids are known to catalyze metal reactions (Denisov, 1974) and so experiments were conducted to examine the effect of naphthenic acids on the decomposition rates of hydroperoxides in the presence of a reactive and a less reactive metal species. The experimental procedure was consistent with the previous studies, in that the metal naphthenate and NA were dissolved in Exxsol D-80 prior to de-oxygenation, heating, and hydroperoxide addition. Hydroperoxide concentrations were monitored over time and the resulting pseudo-first order rate constants are listed in Table 11. The unassisted, metal only assisted, and acid only assisted data for CHP decomposition shown in Table 11 have been reproduced from previous tables to aid data interpretation. The data in the table clearly show that the combination of metal and acid produce a synergistic increase in the decomposition rate of hydroperoxide for all of the temperatures, metal species, or hydroperoxide species examined. This synergistic effect can be illustrated by examination of the CHP decomposition data at 125°C, whereby, addition of either NA or

Zn-na alone has little effect on the relative rate constant of CHP decomposition, while the addition of both NA and Zn-na increases the relative rate constant by a factor of three.

Table 11. Rate Constants for Liquid Phase Hydroperoxide Decomposition with Metal Naphthenates and Naphthenic Acids

RO_2H	T (°C)	Metal Species	[Metal] (mM)	[NA] (mM)	k (10^{-6}/s)	k/k_o
CHP	105	-	-	-	3.5	-
		-	-	0.128	9.2	3
		Cu-na	0.013	-	110	30
		Cu-na	0.013	0.128	2,700	768
	125	-	-	-	22	-
		-	-	0.128	16	0.7
		Cu-na	0.013	-	200	9
		Cu-na	0.013	0.128	9,200	418
		Zn-na	0.012	-	18	0.8
		Zn-na	0.012	0.128	74	3
EBHP	125	-	-	-	85	-
		-	-	0.128	61	0.7
		Cu-na	0.013	-	830	10
		Cu-na	0.013	0.128	12,100	143

Having shown the synergistic effects on RO_2H decomposition of organic acids, in the presence of dissolved metals, results will now be presented regarding the study of one possible mitigation strategy. The jet fuel community has long used metal deactivator additive (MDA) as a means to reduce the reactivity of dissolved metals, mainly copper, in an effort to improve fuel thermal stability. While it is known that MDA chelates dissolved metals, typically resulting in a net decrease in fuel deposition and oxidation rates, specific examples of the affected chemical pathways are not well documented. To this end, experiments were conducted with combinations of Cu-na, NA, and MDA, under conditions identical to those previously reported herein, to test if MDA has an effect on the metal assisted, weak acid assisted, and acid-metal assisted hydroperoxide decompositions. The MDA was added at a concentration of 5.0 mg/L (0.018 mM) and the resulting pseudo-first order rate constants are shown in Table 12. The experimental data generated without MDA has been reproduced from previous tables for ease of interpretation. The data shows that the presence of MDA almost eliminates any increase in the relative rate constant for CHP decomposition due to the addition of NA, Cu-na, or both NA and Cu-na. This demonstrates that MDA does effectively reduce the ability of dissolved metal species to assist in hydroperoxide decomposition, even in the presence of organic acids.

Table 12. Rate Constants of Liquid Phase CHP Decomposition at 125°C

Table [Cu-na] (mM)	[NA] (mM)	[MDA] (mM)	k (10^{-6}/s)	k/k_o
-	-	-	22	-
-	-	0.018	35	1.6
0.013	-	-	200	9
0.013	-	0.018	24	1.1
0.013	0.128	-	9,200	418
0.013	0.128	0.018	28	1.3

Hydroperoxide Decomposition and Deposition

Quartz crystal microbalance (QCM) experiments were performed in which the effect of hydroperoxide decomposition on deposition was isolated. A JP-8 fuel (POSF-4751) was sparged with inert gas to remove dissolved and headspace oxygen and subsequently heated to 140°C. Upon stabilization at this temperature, cumene hydroperoxide was added via syringe to a concentration of about 16 mM. The deposition was followed via monitoring of the crystal frequency in time. Figure 11 shows results for the neat fuel, with added copper naphthenates (~1 ppm copper) and MDA (5.8 mg/L). The figure shows that the neat fuel produced relatively low deposition (<1 μg/cm^2) upon addition, and subsequent decomposition, of the hydroperoxide. The addition of copper increased the initial deposition rate as well as the final deposition quantity demonstrating that the catalytic effect of copper on hydroperoxide decomposition (and possibly deposition reactions) results in an increased deposition rate. The time for leveling of the deposition is also earlier than for the neat fuel. The addition of MDA to the fuel/copper mixture results in a slowing of the initial deposition rate but the rate is still higher than the neat fuel. MDA also results in an increase in the final deposit quantity. Thus the ability of MDA to deactivate copper catalysis does result in a decreased deposition rate during hydroperoxide decomposition, but the deposition rates and final quantity is higher than the neat fuel.

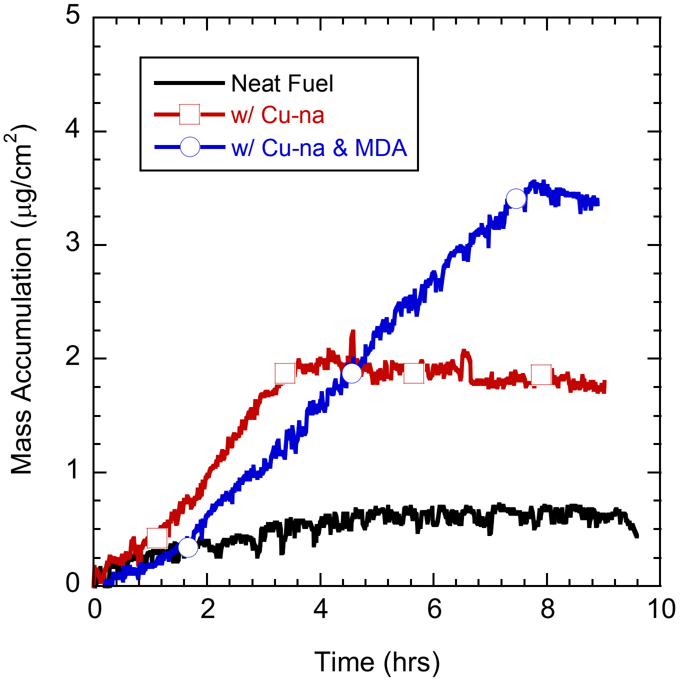

Figure 11. Plots of QCM deposition vs. time for fuel POSF-4751, with added copper naphthenates (~1.0 ppm copper), and MDA (5.8 mg/L).

Figure 12 shows the results for addition of naphthenic acids to the fuel/hydroperoxide system. The acids result in an increased initial deposition rate and final deposit quantity, similar to the behavior observed for the addition of copper (Figure 11). This substantial increase in deposit quantity and rate is surprising considering that the data in Table 10 show only a modest catalytic effect of the acid mixture on CHP decomposition in this temperature range. The addition of MDA to the naphthenic acid/fuel/hydroperoxide system results in a slowing of the initial deposition and a decrease in the final deposit quantity. It is also interesting that MDA has such a strong effect on the observed acid catalysis of hydroperoxide decomposition, as it is normally expected to only play a role in mitigating metal catalysis. While the dissolved metal content of fuel POSF-4751 is quite low, the QCM reactor, crystal adapter, and crystal electrode all consist of surface metals which may interact with the MDA and result in surface catalysis deactivation.

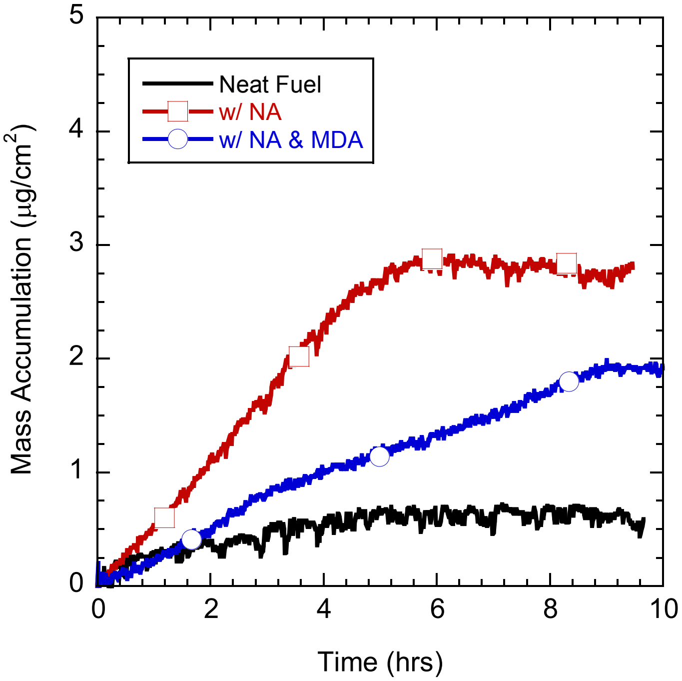

Figure 12. Plots of QCM deposition vs. time for fuel POSF-4751, with added naphthenic acids (~1 ppm wt), and MDA (5.8 mg/L).

As synergism was observed above in the combined effect of copper and acid on hydroperoxide decomposition rates, it becomes of interest to study if this synergism extends to deposition rates as well. Therefore, copper and acid were combined in jet fuel and thermally stressed to monitor deposition rates during hydroperoxide decomposition. The results in Figure 13 show that the initial deposition rate is only slightly higher than either copper or acid alone, demonstrating that synergism does not play an important role in the deposition process during hydroperoxide decomposition. In addition, the final deposit quantity in the presence of both copper and acid is not significantly higher than the runs with only the acid added (Figure 12). The addition of MDA to the combined copper/acid fuel results in a reduction of the deposition rate, but the final deposit amount remains unchanged.

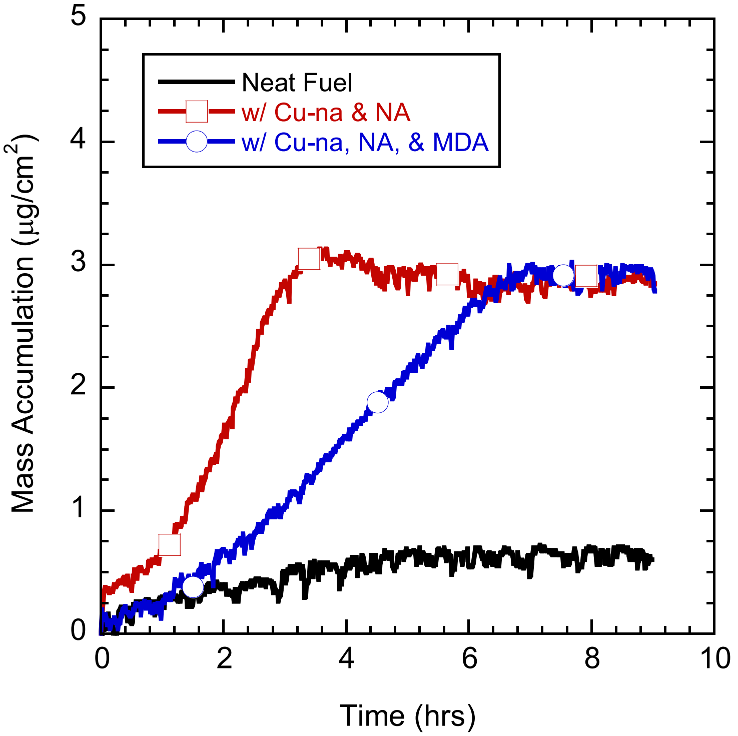

Figure 13. Plots of QCM deposition vs. time for fuel POSF-4751, with added naphthenic acids (~1 ppm wt) and copper naphthenates (1.0 ppm copper), and MDA (5.8 mg/L).

Interpretation of Results

Hydroperoxides, which are formed during jet fuel autoxidation from the bulk fuel components, can be relatively stable at lower temperatures but at higher temperatures become a significant source of radical production. As jet fuel is a complex mixture of normal-, iso-, and cyclo-paraffins, as well as alkyl aromatics, hydroperoxides of various types can be formed in real jet fuel oxidation. The propensity for hydrogen abstraction, and thus subsequent hydroperoxide formation, of a given fuel hydrocarbon depends on both the bond strength and steric factors of the C-H bond. Zabarnick and Phelps (2006) calculated that abstraction of benzylic hydrogen from alkyl aromatic species has an E_a of at least 4-5 kcal/mol lower than abstraction of paraffinic hydrogens, making alkyl aromatic species, e.g., ethylbenzene and cumene, likely species that readily produce fuel hydroperoxides. In this study, n-dodecane and ethylbenzene were oxidized separately, under mild conditions, to produce the subsequent hydroperoxides (Chapter II). It was found that the ethylbenzene readily produced hydroperoxides at 80°C whereas the n-dodecane required a higher temperature, 100°C, to produce any significant quantity of hydroperoxide over a similar reaction time period. The higher yield of EBHP compared to DHP is experimental evidence supporting the assertion that species with weaker benzylic hydrogen bonds, e.g., ethylbenzene, are more likely to form hydroperoxides under typical jet fuel thermal oxidation conditions. Therefore, CHP represents a relevant model fuel hydroperoxide since it is a jet fuel distillation range alkyl aromatic hydroperoxide.

The study of CHP decomposition under conditions representative of jet fuel thermal stability has some precedent. Mushrush et al. (1994) observed the thermal decomposition products of CHP from 130 to 170°C in benzene, and from this chemical analysis determined that the predominant reaction pathway must be homolysis of the O-O bond in the hydroperoxide. A wide variety of decomposition products were noted in the study including trace carboxylic acids. Unfortunately, the activation energy was not determined for the CHP decomposition reaction. The activation energy measured in this work for the decomposition of CHP in Exxsol D-80 was 23±3 kcal/mol (Table 7) and is in good agreement with a previous study which determined a value of 25.4 kcal/mol (Nurullina et al., 2006). The CHP thermal decomposition studies of Mushrush et al. (1994), Nurullina et al. (2006), and this work were conducted in the liquid phase, which is relevant to the autoxidation of jet fuel in real fuel systems. However, the observed liquid phase Ea of about 23-25 kcal/mol for CHP thermal decomposition is much less than the average gas phase Ea values of about 43-45 kcal/mol for most hydroperoxides (Benson, 1981; Denisov & Denisova, 2000). One possible argument to account for the large differences noted in the gas and liquid phase activation energies is not the reaction phase, but rather that the R group has an impact on the O-O bond strength. The gas phase Ea, typically used for combustion modeling, is for an alkyl hydroperoxide, not an alkyl aromatic (or benzylic) hydroperoxide. Indeed it has been shown that the R group can alter the O-O bond strength significantly, whereby the bond energy is reduced by as much as about 20 kcal/mol when R is a vinyl or phenyl group compared to an alkyl group (Sebbar et al., 2002). However, DHP also gives a liquid phase Ea for thermolysis of 24 kcal/mol, which refutes the previous argument. One possible explanation for the disparity between the liquid and gas phase activation energies is that cage effects are present in the liquid phase thermolysis of hydroperoxides. Cage effects are well known in liquid phase decompositions and have been demonstrated to affect the reaction rate constants of similar liquid phase reactions (Denisov, 1974; Pryor & Smith, 1970). The presence of cage effects may lower the apparent unimolecular liquid phase Ea of hydroperoxide thermolysis and also decrease the frequency factor. Gas phase unimolecular thermolysis has a frequency factor of about 10^{13} to 10^{16} s^{-1} (Gardiner, 1972); whereas, the measured liquid phase frequency factor was shown to be about 10^{7} to 10^{10} s^{-1} for this work (Table 7) and about 10^{9} s^{-1} for Nurullina et al. (2006). The large difference in both the E_a and the frequency factor is a significant issue when selecting values to be used for modeling purposes, as the more common gas phase values have typically been used in pseudo-detailed computations, whereas the liquid phase values may be more appropriate in light of the current findings.

An effect that has been recently incorporated into pseudo-detailed chemical mechanisms is the catalytic decomposition of hydroperoxides via a single bimolecular reaction involving a catalytic dissolved metal species and a hydroperoxide to produce two radicals (Kuprowicz et al., 2007). Interestingly, the dissolved metals selected to incorporate into the model were Cu and Mn, while Fe, Mg, and Zn were excluded from the model. The authors' decision to include just these two dissolved metals, of the five that were quantified, was based upon the relatively large sensitivity of the model to the measured Cu and Mn concentrations of the fuel samples. As was shown above experimentally (Table 8 and Table 9), both Cu and Mn naphthenates have a strong effect on the E_a of hydroperoxide decomposition. Additionally, it was shown that Fe and Zn appear to have little effect on the E_a for hydroperoxide decomposition. Both iron and zinc have been reported to increase the overall oxidation rate of jet fuels, however, only at much higher concentrations (Hazlett, 1991). Thus the mode of action of iron and zinc may influence some other portion of the autoxidation chain, or the metals may simply require higher concentrations to affect the hydroperoxide decomposition step.

It was previously mentioned that transition metals are currently believed to take the form of organometallic salts, such as metal naphthenates, when dissolved in jet fuel; however, there is little understanding of the role of the ligand in metal catalysis of hydroperoxide decomposition. Therefore, copper bis(2,2,6,6-tetramethyl-3,5-heptanedioate) (Cu-tmhd) was chosen as a comparison species to Cu-na. The results in Table 8 clearly show that the organic ligand has an effect on the relative reaction rates of the two copper species, i.e., the hindered dioate complex (Cu-tmhd) tends to reduce the severity of catalytic hydroperoxide decomposition compared to the naphthenate complex (Cu-na). These results lead to the conclusion that organometallic speciation, rather than metal atom analysis, is important in determining the potential extent of catalysis of hydroperoxide decomposition. In contrast, the recently adopted approval process for alternative jet fuels (ASTM D4054) employs quantitative analysis of individual metal atoms rather than metal speciation.

Quantification of dissolved metals in petroleum-derived jet fuel is not currently required by specification, let alone the speciation of organometallic compounds; however, the total acid number (TAN) is a required specification property for jet fuel. Even though the TAN specification limit for JP-8 fuel is relatively low (0.015 mg KOH/g), as was shown above the effects of a small (within specification) amount of acid, in the presence of dissolved metal, can have a synergistic effect on the decomposition rate of hydroperoxides (Table 11). The synergistic increase in decomposition rate is significant when either a reactive metal, such as Cu, or a less reactive metal, such as Zn, are present with naphthenic acids. The mechanistic details of synergism are poorly understood, but the acid may affect the oxidation state of the metal during hydroperoxide decomposition, making the metal more reactive in encouraging hydroperoxide decomposition. Another possible explanation relates to the earlier mentioned concept that dissolved metal species may not be true catalysts during jet fuel autoxidation. Rather, instead of the metal ion being regenerated after hydroperoxide decomposition, Zabarnick and Phelps (2006) proposed the formation of a metal complex, which for the case of divalent copper is $CuOH^{+2}$. The acid may act to help regenerate a more reactive form of the metal, thus increasing the hydroperoxide decomposition rate. Regardless of the mechanism, the concept of acid/metal catalysis has far reaching implications with regard to jet fuel handling and thermal stability. One unfortunate scenario would involve a high metal containing fuel that accumulates organic acids during storage. It is feasible that this hypothetical jet fuel initially has good thermal stability; however, upon storage, and subsequent acid accumulation, becomes a fuel with poor thermal stability. Therefore, it is useful to consider mitigating strategies to prevent this synergistic increase in hydroperoxide decomposition.

It has been known for some time that MDA has the ability to improve the overall thermal stability of jet fuels containing reactive dissolved metals (Waynick, 2001). As with many jet fuel studies, the global impact of MDA on thermal stability is often the only cited result. This methodology prevents a fundamental understanding of the chemistry; and therefore, prevents the ability to predict this important fuel chemistry. The results shown in Table 12 provide insight into one chemical pathway that is strongly affected by the presence of MDA, i.e., metal assisted hydroperoxide decomposition. The ability of MDA to strongly complex with Cu effectively renders the dissolved metal unreactive with respect to catalyzing hydroperoxide decomposition. Since MDA is able to "turn off" this lower activation energy pathway to hydroperoxide thermolysis, and MDA has been shown to improve jet fuel thermal stability, the evidence shows the importance of hydroperoxide decomposition to the overall fuel thermal stability.

Isolation of the role of hydroperoxide decomposition in jet fuel deposit formation was performed in the QCM studies reported here. The results indicate that hydroperoxide decomposition in the absence of oxygen does result in significant surface deposition. Thus, hydroperoxides can be thought of as a stored form of oxygen. Their decomposition "releases" oxygen radicals which initiates a reaction process resulting in deposit formation. This process may differ from the deposition process which occurs during autoxidation, as the absence of oxygen will result in differing reaction pathways. In particular, peroxy radicals, which are the main chain carrier during autoxidation, will not exist in these hydroperoxide decomposition experiments. In addition, during autoxidation oxygen readily adds to radical sites. This oxygen addition likely occurs during deposit forming reactions. In these hydroperoxide decomposition experiments this oxygen addition will not occur. Thus it is likely that the deposition pathways that occur during hydroperoxide decomposition in the absence of oxygen differ from those that occur during autoxidation, except for the period of autoxidation near complete oxygen consumption. These low oxygen, hydroperoxide decomposition deposition pathways may also occur at some limited oxygen locations within fuel systems.

The QCM studies also point out differences in the behavior of added copper, acid, and MDA on hydroperoxide decomposition rates and deposition rates. Copper strongly catalyzes hydroperoxide decomposition and in turn results in increases in deposition rates and final deposit quantities. The addition of naphthenic acids has a minimal effect on hydroperoxide decomposition, but a significant effect on increasing deposition rates and final deposit quantities. Copper and acid exhibit significant synergism in increasing hydroperoxide decomposition rates but do not show synergism in effects on fuel deposition rates or final deposit quantities. MDA slows deposition rates due to copper, acid, and the copper/acid combination but does not always decrease final deposit quantities. These QCM deposition studies show the complex behavior and mechanisms during autoxidation and hydroperoxide decomposition. Future studies may be able to further elucidate these mechanisms and enable novel deposit mitigation schemes.

CHAPTER IV

EFFECTS OF LAMINAR & TRANSITIONAL FLOW HIGH FLUX HEAT TRANSFER ON JET FUEL AUTOXIDATION & DEPOSITION

Introduction

Jet fuel used for regenerative cooling of hypersonic vehicles is exposed to very high surface temperatures for short periods of time. These extreme heat transfer conditions lead to the development of high heat fluxes and large thermal gradients. Figure 14 shows that many physical conditions are coupled, i.e., reliant upon each other, often non-linearly. For instance, temperature directly affects many physical properties non-linearly, e.g., density and viscosity (Appendix B). Additionally, Arrhenius reaction rate constants are an exponential function of temperature. The fluid flow conditions, e.g., Re, are affected by fluid properties, which defines the heat transfer coefficients. Heat transfer can also be affected by chemical reactions, in that surface deposits have a low thermal conductivity and will foul heat transfer surfaces; therefore, reducing local heat transfer coefficients. When large extents of reaction occur, e.g., pyrolytic fuel cracking with percent level liquid-to-gas conversion, the chemical constituents of the fuel can change dramatically. Dramatic shifts in bulk composition can affect the fuel physical properties. Additionally, some fuel cracking reactions can be endothermic, which directly impacts the fuel temperature. With such high levels of non-linear coupling, even relatively simple heat transfer scenarios can benefit from computational analysis to help resolve and analyze the physical phenomena.

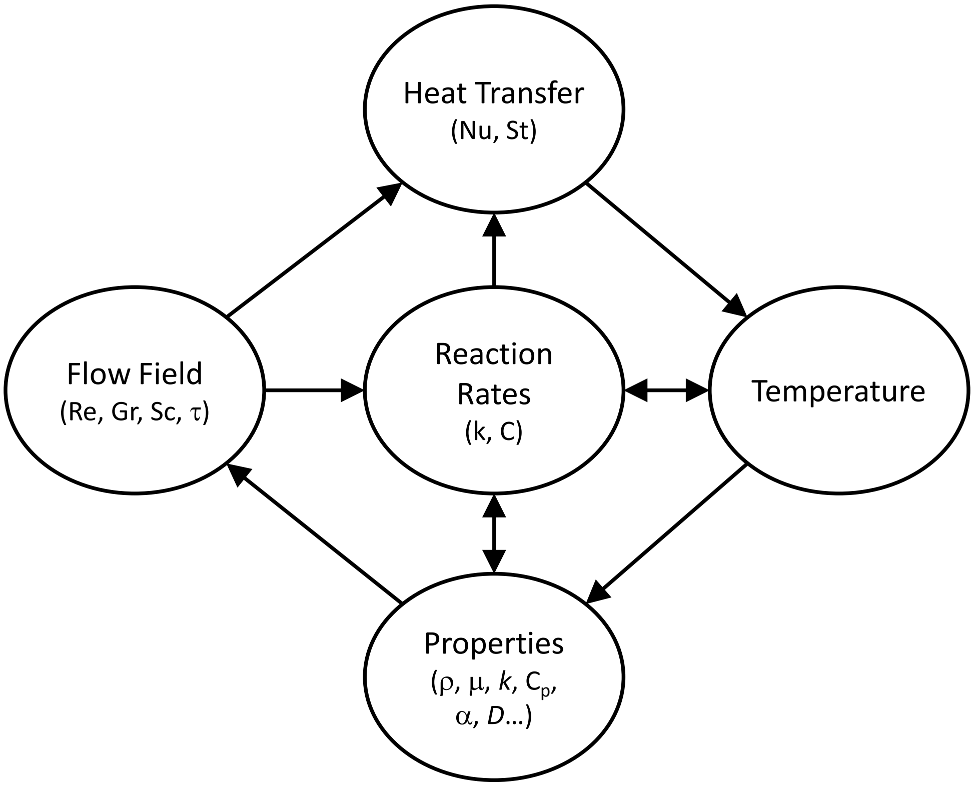

Figure 14. Diagram of physical phenomena coupling.

This chapter reports on the experimental observations of two, relatively simple high flux heat transfer scenarios: the first involves heat transfer to a laminar fluid in a straight tube, and the second involves a fluid that transitions from laminar to turbulent flow due to heating of the fluid in a straight tube. Computational fluid dynamics (CFD) with chemistry will be used to simulate the fuel conditions within the heated tube to provide insight into the fluid dynamics, heat transfer, and chemical kinetics of the corresponding experimental cases. A brief discussion of the chemical mechanism used in the computations will be followed by experimental results and discussion.

Chemical Mechanism

As indicated in Chapter I, a pseudo-detailed chemical mechanism has been successfully implemented previously by Kuprowicz et al. (2007) for lower temperature and lower heat flux conditions than the present study. The intention for the present study was to examine the usefulness of the pseudo-detailed chemical mechanism under more severe conditions with as little adaptation as possible. Therefore, the pseudo-detailed chemical kinetic mechanism used for the current work (Table 5) contains only a few revisions of the Kuprowicz et al. (2007) mechanism. The most significant modifications include: the addition of a high temperature oxidation pathway (reaction 17); the addition of a high temperature radical initiation pathway (reaction 27); the inclusion of a sulfur deposition pathway (reactions 24 through 26); and revised Arrhenius parameters for hydroperoxide decomposition (reaction 8 and 9). The high temperature oxidation pathway (reactions 17 through 20) is based on work reported by Benson (1986) and is relevant to high temperature oxygen consumption for both gases and liquids. The revised hydroperoxide decomposition parameters (reactions 8 and 9) were based upon the results reported in Chapter III and by West et al. (2011). The high temperature radical initiation step (reaction 27) represents a possible pyrolytic radical initiation pathway of a fuel heteroatomic species due to the elevated surface temperatures of this study. And the sulfur deposition pathway (reactions 24 through 26) is based on the empirical deposition pathway (reactions 21 through 23) developed by Kuprowicz et al. (2007) with the same

Arrhenius parameters being used to compare the two mechanisms directly. Kuprowicz et al. (2007) investigated the use of such a sulfur deposition pathway, yet determined it to be an insignificant contributor to deposition for the less severe conditions examined, i.e., maximum wall temperatures of ≤ 400°C. Finally, the generic radical initiation reaction, I → R·, was removed from the previous mechanism since radical generation via hydroperoxide decomposition is significant enough to initiate autoxidation.

Laminar Flow Condition

JP-8 jet fuel was thermally stressed in an electrically heated tube apparatus as described above in the experimental section (Chapter II). Two case studies will be examined with the first, Case A, being the simpler of the two with respect to flow field and severity of heat transfer conditions. The electrical power supplied to the test specimen for Case A, 0.35 Btu/s (0.37 kW), was enough to raise the exiting bulk fuel temperature to 65°C (Table 13). The slight increase in bulk fuel temperature increased the outlet Re to about 2,500, while the inlet Re was about 1,600, indicating that the flow remained laminar throughout the heated tube. Figure 15 shows the measured outer wall temperature profile of Case A versus normalized tube length, L/D (length divided by tube diameter). The figure shows a continued rise in the wall temperature until the end of the heated zone, L/D ≈ 60, where a maximum wall temperature of about 660°C is observed. This temperature profile is consistent with a constant heat flux, laminar flow heat transfer process (Incropera et al., 2007). The relatively low bulk outlet fuel temperature, even with the high wall temperatures, is mostly due to the short fuel residence time, ~90 ms, in the heated zone. That is, the energy transfer into the fuel is small compared to the high fuel mass flow rate and high fuel specific heat, C_p. Table 13 also lists the measured bulk outlet oxygen concentration, which shows that only limited oxygen consumption occurred, with 94% remaining at the tube outlet.

Having established that Case A is laminar flow through the heated zone, the numerical analysis was simplified by using the well defined laminar flow model as opposed to a turbulent flow model. The remaining experimental conditions of Case A were modeled using CFD with chemistry as described in the numerical section (Chapter II). Scheme 1 was used to define the energy boundary conditions for Case A, where $q''' =$ 10.5 Btu/s- in^3 (6.77×10^8 W/m^3). The source term, q''', represents the electrical resistance heating within the stainless steel tubing. Figure 15 shows the numerically simulated temperature profiles with respect to normalized radial distance, r/R (radial position divided by inner wall radius). Assuming minimal thermal resistance in the metal tube, the figure shows good agreement between the measured outer and simulated inner wall temperatures, which gives confidence to the numerical results. Additionally, the simulated bulk outlet temperature, 69°C, is in good agreement with the experimentally measured value, 65°C (Table 13). Figure 15 also shows the very large radial temperature gradients within the heated zone of the tube, from L/D of 0 to about 60, by examining the temperature profiles at various r/R. For instance at an L/D of 50 the fluid temperature drops from 637°C at the wetted wall, r/R = 1.0, to 341°C at five percent from the wetted wall, r/R = 0.95, for a ΔT of 296°C. Additionally, the centerline fuel temperature remains nearly unchanged, about ambient temperature, while the maximum wetted wall temperature reaches about 660°C over a distance of only 0.0425 in! The fuel transitions to a supercritical fluid at temperatures above the pseudo-critical temperature, $T_{pc} \approx$

500°C, where it experiences a large change in physical properties such as a decrease in the fluid density and viscosity (Appendix B). Two-phase fluid flow (supercritical fluid and sub-critical liquid) can cause flow instabilities and lead to unstable control regimes (Linne et al., 2000). However, the dramatic pressure oscillations indicative of such flow instabilities were not observed for either Case A or Case B.

Table 13. Experimental and Numerical Bulk Outlet Data

Bulk Outlet Property	Case A	Case B
Temperature (°C)		
Measured	65	163
Computed	69	202
Oxygen (%Sat)		
Measured	94	72
Computed	94	93

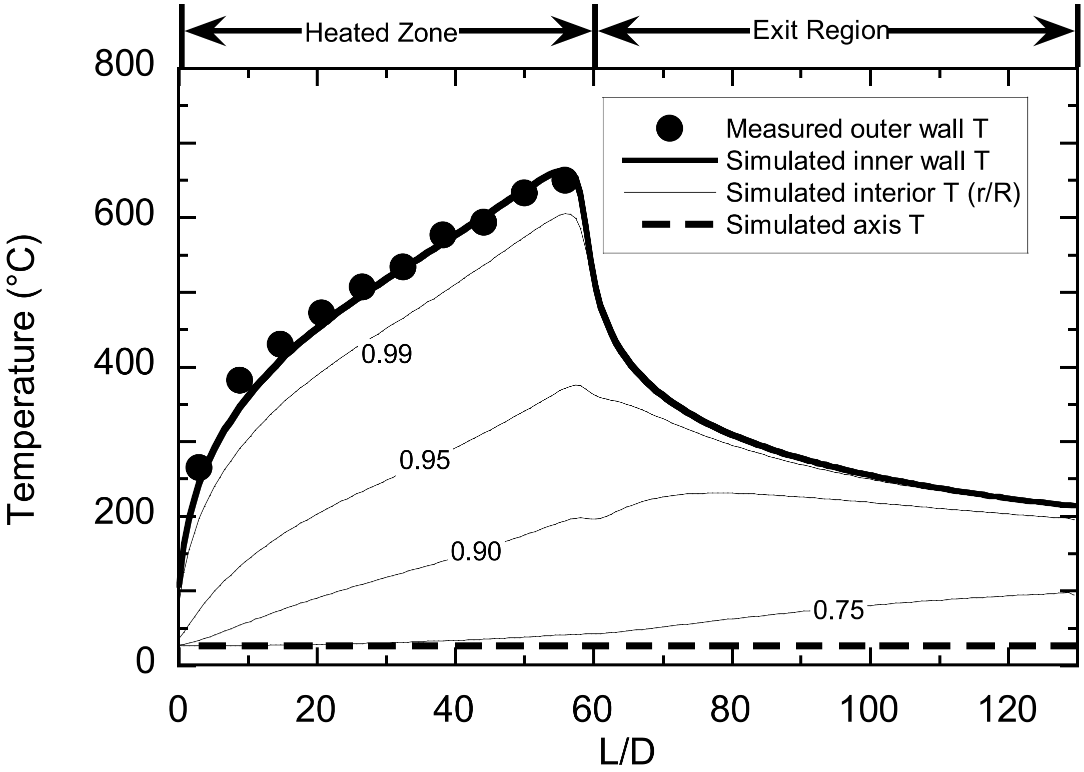

Figure 15. Temperature profiles for Case A: markers represent thermocouple measurements, solid and dashed lines represent simulated results at a given normalized tube radius (r/R).

In addition to fluid and heat transfer analysis, a pseudo-detailed autoxidation mechanism (Table 5) was incorporated into the simulation. Figure 16 shows the resulting contours of relative dissolved oxygen near the wall, r/R ≥ 0.75, for Case A. As the figure shows, oxygen is completely consumed in the hottest portion of the fluid, i.e., near the wall at the exit portion of the heated zone. However, this layer of oxygen depleted fluid is quickly replenished via diffusion in the exit region of the tube, L/D ≥ 60. The observation of localized oxygen depletion (Table 13 and Figure 16) has implications on how fuel might be managed within the aircraft fuel control loop. That is, maximum oxidative deposition rates are expected to occur near such an area of oxygen depletion due to the inverse relationship between oxidation and deposition reactions (Zabarnick, 1994), and will be confirmed later in the discussion. Relative oxygen concentration can be seen as the remaining "deposit potential" of a fuel. Since the Case A bulk fuel oxygen concentration changes very little, the exiting fuel still has "deposition potential" and can continue to deposit later on in a fuel control loop if re-exposed to high temperatures.

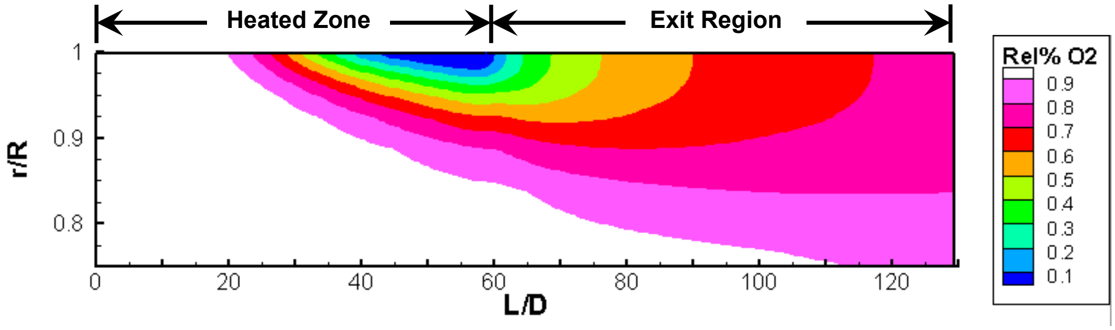

Figure 16. Relative percent oxygen contour for Case A.

Another species of interest, due to its importance in the autoxidation mechanism as an intermediate and radical initiation source, are hydroperoxides. Figure 17 shows simulated hydroperoxide, RO_2H, mole fractions for Case A. It can be seen in the figure that the RO_2H level at the wall first increases, reaching a maximum at an L/D of ~30 (T ≈ 517°C), then decreases to a minimum level just before L/D = 60 (T ≈ 657°C). Similar to that of oxygen, the RO_2H level at the wall is replenished soon after the heated zone where L/D ≥ 60. However, the RO_2H levels at radial positions farther away from the wall, e.g., $r/R < 0.9$, tend to only increase in amount, i.e., RO_2H production is always greater than RO_2H destruction for the residence times and temperatures in this 'bulk' portion of the flow. Similar to low levels of bulk oxygen consumption corresponding to low levels of total fuel oxidation, the net production of RO_2H signifies that only small extents of chemical conversion are occurring in Case A. The exception is, again, in the hot fluid film near the heated zone exit where RO_2H concentration decreases. Nevertheless, the overall increase seen in the simulated RO_2H concentration could prove to accelerate oxidation and deposition rates should the fuel be re-circulated within a heated control loop.

The oxygen and RO_2H results (Figure 16 and Figure 17) demonstrate the ability to achieve fine special resolution of species levels within the flow field, but reaction rates are also informative of chemical activity within the reacting fluid. For example, Figure 18 shows contours of the volumetric reaction rates for reaction numbers 7 and 14 (Table 5). The figure shows that reaction number 7 ($A\cdot + RO_2\cdot \rightarrow \text{Products}_{AH}$) reaches a maximum rate at a distance of about 5% from the wall, $r/R \approx 0.95$. In contrast, reaction number 14 ($RO_2H + SH \rightarrow \text{Products}_{SH}$) reaches a maximum rate at the wall, $r/R = 1.0$. The observation that these two reaction rates reach a maximum at different locations within the flow field means that they are sensitive to more than just temperature. These reactions both produce deposit precursors via different pathways. The rate of reaction number 7 depends on the concentration of two intermediate radical species and has no activation energy, where the rate of reaction number 14 depends on the concentration of two stable molecular species and has an E_a = 18 kcal/mol. Since deposit precursors must migrate to a surface in order to form deposits, the precursors formed closer to the wall will have less distance to travel to the surface and thus be more likely to form surface deposits. This also emphasizes the notion that reaction rates are sensitive to both concentration and temperature, which are complex functions of other factors (Figure 14).

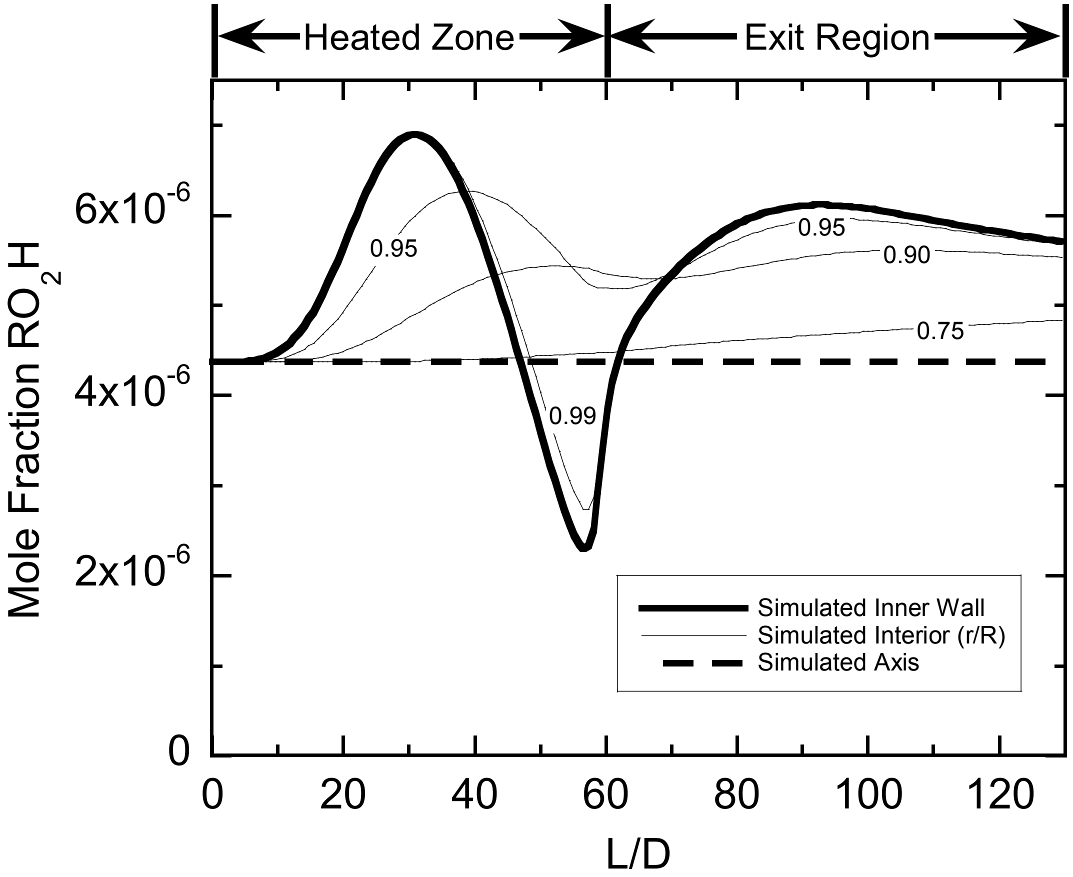

Figure 17. Simulated RO_2H mole fractions at various radial locations for Case A.

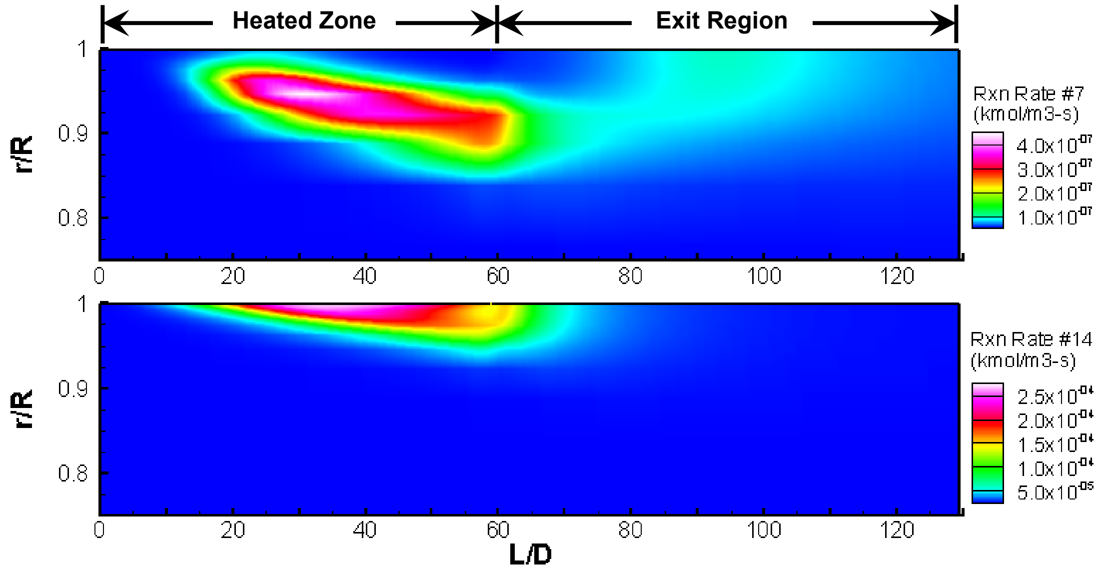

Figure 18. Contours of reaction rate (a) #7 and (b) #14 for Case A.

Fuel species concentrations, reaction rates, and temperature profiles have been shown for a laminar flow heated tube (Case A) and, as was observed, the reaction kinetics were coupled to the flow conditions. Depending on the geometry and transient mass flow requirements, real aircraft fuel systems can operate under laminar or turbulent flow conditions (CRC, 1991). Therefore, a heat induced transitional flow case (Case B), with a laminar inlet (Re = 1,700) and turbulent outlet (Re = 5,900), was examined both experimentally and numerically to further investigate the effect of flow dynamics on the chemical mechanism. The measured bulk outlet temperature for Case B was 163°C and the measured bulk outlet oxygen concentration was 74% of air saturated fuel (Table 13). The higher level of oxygen consumption in Case B is due to the 100°C higher bulk outlet temperature and a residence time double that of Case A, ~180 ms (Table 3). Figure 20 shows the experimentally measured wall temperature profile versus L/D for Case B. The figure shows a dramatic decrease in wall temperature from L/D of about 20 to 50 even though the actively heated portion of the tube is from L/D of 0 to about 120. This reduction in temperature contrasts with that of Case A (Figure 15), where the temperature continues to increase until the end of the heated zone. The cause of this temperature reduction will be discussed in detail below.

Transitional Flow Condition

Before numerical simulations could be conducted for Case B, an appropriate viscous model had to be selected. Four different turbulence models were considered including: standard κ-ε (SKE), renormalized group κ-ε (RNG) with EWT, Reynolds stress model (RSM), and SST-κ-ω turbulence models (ANSYS, 2010a). The Scheme 1 boundary conditions (Chapter II) were applied with q''' = 20 Btu/s- in^3 (1.29×10^9 W/m^3) for all four turbulence models. Figure 19 shows the resulting predicted outer wall temperature profiles using the four different turbulence models along with the experimental measurements. Even thought the SKE model has been used successfully in the past for fuel heat transfer predictions (Katta & Roquemore, 1993), the figure shows that both the SKE and RSM models under-predict the measured outer wall temperatures. More recently, the RNG-EWT model was shown to be more effective under fully turbulent, high heat flux heat transfer conditions (Jiang, 2011). However, Case B transitions from laminar to turbulent flow, which the RNG-EWT model does not predict according to turbulence intensity data (not shown). The SST-κ-ω model can be used as a rudimentary transitional flow model (ANSYS, 2010b) and also shows reasonable agreement with the experimental data (Figure 19); therefore, the SST-κ-ω turbulence model was selected for all subsequent numerical analysis.

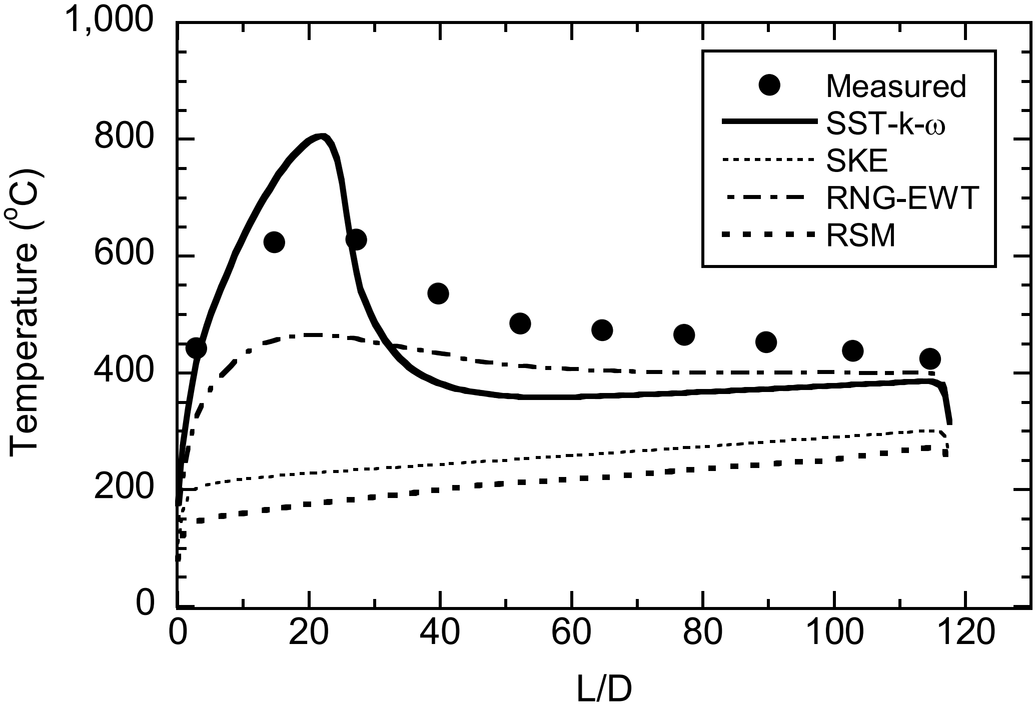

Figure 19. Outer wall temperature profiles for Case B using various turbulence models.

Even though Scheme 1 boundary conditions were used to select a turbulence model, Scheme 2 boundary conditions were used for subsequent numerical computations of Case B involving chemistry. Thus, the measured outer wall temperature was fit to the heated zone in the computations to better represent the temperature conditions within the flow field. Figure 20 shows the measured outer wall temperatures and numerically simulated temperature data at various r/R for Case B. The figure shows that the maximum measured wall temperature occurs near the inlet of the heated zone, at an L/D of about 20. This observation is in contrast to the results of Case A where the maximum temperature was near the exit of the heated zone. To help explain this, Figure 21 shows the turbulent intensity of the fluid for Case B. The figure shows that the fuel transitions from laminar to turbulent flow around L/D of about 30 to 50. Since heat transfer is more effective under turbulent conditions, i.e., the heat transfer coefficient is larger at higher Reynolds numbers, it stands to reason that a decrease of the tube wall temperature would correlate to the flow conditions shown in Figure 21. Thus the reduction in measured tube wall temperature, as seen in Figure 20, is attributed to the transition of the flow from laminar to turbulent within the constant heat flux experiment. Additionally, Figure 20 shows that the temperature difference between the wall (r/R = 1.0) and 1% into the fluid (r/R = 0.99) actually increases in the turbulent section, i.e., the temperature difference, $\Delta T = T_{r/R=1.0} - T_{r/R=0.99}$, is about 100°C at L/D of 20 (laminar flow) and the ΔT is about 150°C at L/D of 60 (turbulent flow). Simply put, the thermal boundary layer thins once the flow transitions from laminar to turbulent.

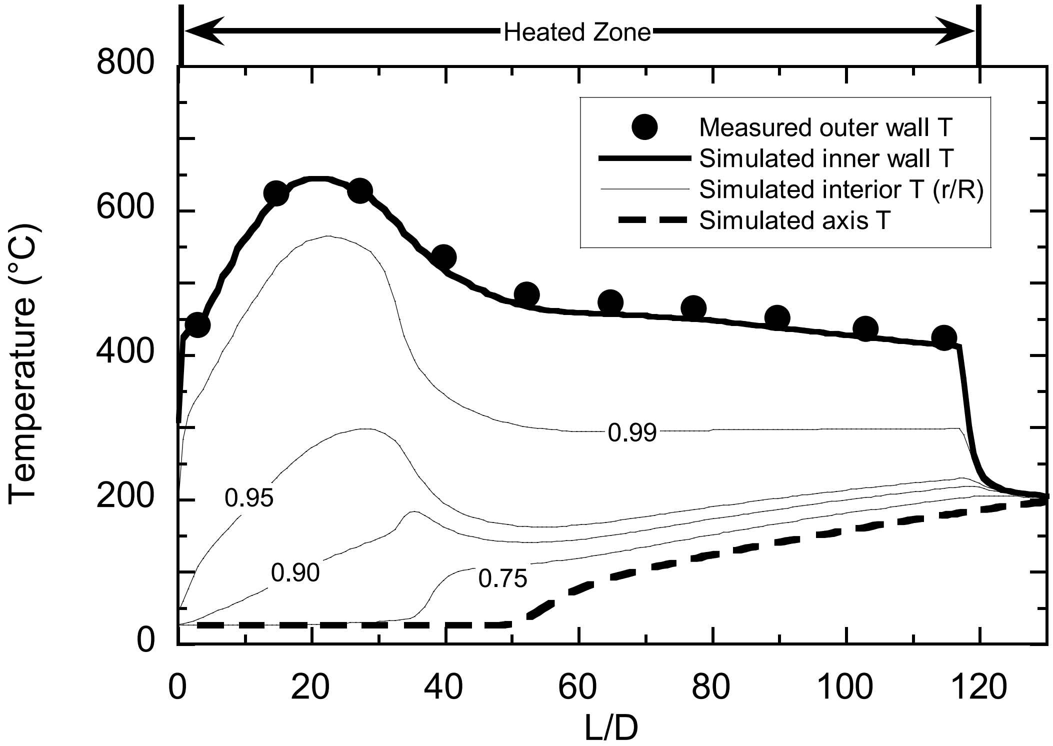

Figure 20. Temperature profiles for Case B: markers represent thermocouple measurements, solid and dashed lines represent simulated results (using the SST-κ-ω turbulence model) with respect to r/R.

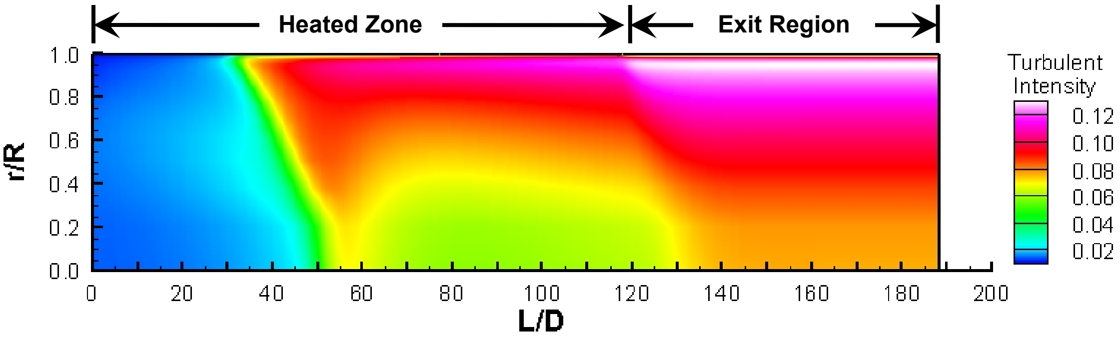

Figure 21. Turbulent intensity contour for Case B.

Now that the temperature and flow conditions have been shown for Case B, it is desirable to examine the effect on species concentrations. Figure 22 shows the relative percent dissolved oxygen for Case B. The figure shows how the oxygen concentration is striated in the laminar section of the tube (L/D ≤ 30), much like Case A, with almost no oxygen very near the wall. However, upon transitioning to turbulent flow (L/D > 30) the near-wall concentration of oxygen is quickly replenished and the radial oxygen concentration becomes more homogeneous. The transition of the flow, from laminar to turbulent, induces bulk fluid mixing and a reduction in the boundary layer thickness, which homogenizes the radial temperature and species concentrations.

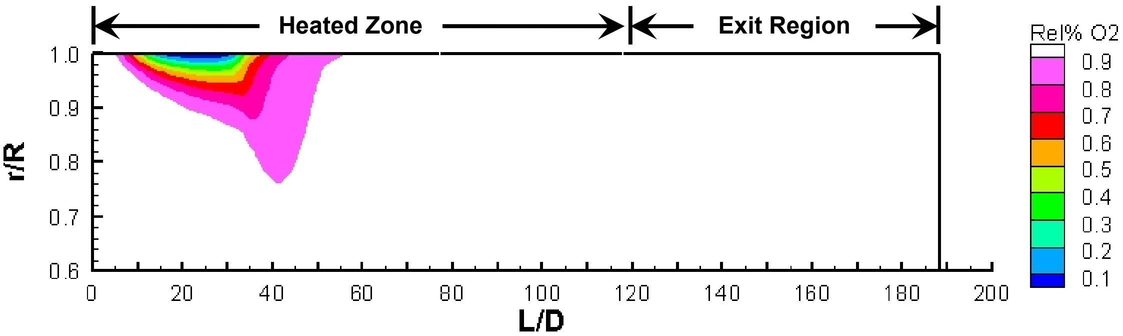

Figure 22. Relative percent oxygen contour for Case B.

This incipient mixing, due to transitional flow, presents a unique opportunity for various chemical species from the model to interact. For example, Figure 23 shows contours of the volumetric reaction rates for reaction numbers 7 and 14. Figure 23 shows results similar to that of Figure 18 in that reaction 7 reaches a maximum rate at a radial position off of the wall, while reaction 14 reaches a maximum rate on the wall. However, the data in Figure 23a and Figure 21 combined show that the maximum rate for reaction 7 occurs where the fluid transitions to turbulent flow. Additionally, reaction 7 extends deeper into the flow field in Case B, making a distinctive L-shape, suggesting turbulent mixing is bringing species from near the wall further out into the flow field. Therefore, the rate of reaction 7 appears to be strongly influenced by turbulence induced optimization of reactant species and temperature. It should also be noted that the maximum reaction rate of reaction 7 for Case B is almost 10 times that seen in Case A, emphasizing the importance of flow conditions on relative reaction rates.

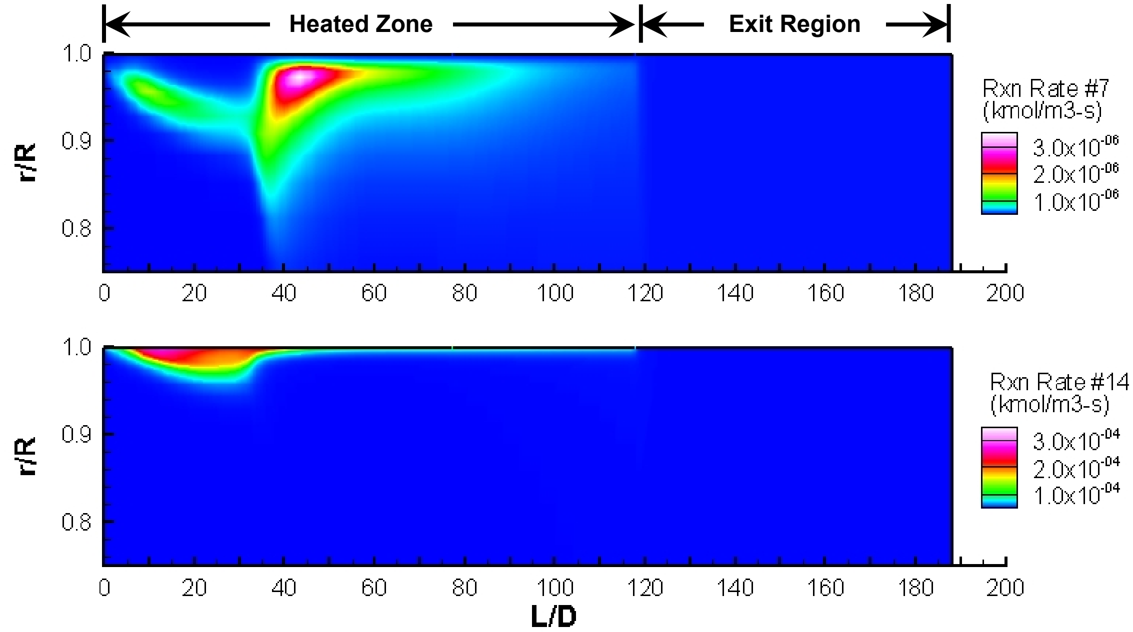

Figure 23. Contours of reaction rate (a) #7 and (b) #14 for Case B.

Deposition Conditions

While explicit chemical mechanisms for jet fuel deposition are not well understood, it has been shown that naturally occurring phenolic species (AH) can be used to simulate experimental deposition results with good agreement at temperatures ≤ 360°C (Kuprowicz et al., 2007). It has also been hypothesized that reaction products of hydroperoxides and reactive sulfur species (SH) such as sulfides and disulfides can lead to deposition (Kauffman, 1997); although previous attempts to correlate SH reaction products with measured deposition was poor for lower temperature thermal stress conditions (Kuprowicz et al., 2007). The current pseudo-detailed chemical mechanism makes use of both deposition pathways: AH derived surface deposits (reaction 23) and SH derived surface deposits (reaction 26). In order to have a more direct comparison between the two deposition pathways, the SH derived deposition pathway (reactions 24 through 26) has identical Arrhenius parameters to those of the empirically derived AH deposition pathway (reactions 21 through 23).

The two model pathways for deposition were compared to experimental results; Figure 24 shows the measured carbon deposit, simulated AH derived deposit, and simulated SH derived deposit for Case A. The figure shows that the measured deposit is relatively low, which is due to the low overall oxygen consumption. Nevertheless, a small deposition peak can be seen near the exit of the heated zone (L/D ≈ 50) where oxygen depletion and net hydroperoxide consumption were predicted near the wall (Figure 16 and Figure 17). A simulated SH deposition peak appears to coincide with the location of the small measured peak; however, these results should be regarded as qualitative since studies must be conducted to calibrate the actual kinetic parameters of the SH deposition pathway. Figure 25 shows the measured and predicted deposition for Case B. Unlike Case A, the figure shows significant deposition peaks for Case B. This increased amount of deposit correlates well with the increased consumption of total oxygen (Table 13). However, the figure shows an unexpected bimodal deposition pattern with deposit peaks at L/D of about 20 and 110. The first deposit peak, at L/D ≈ 20, coincides with the maximum wall temperature (Figure 20) and the local zone of oxygen depletion (Figure 22), which is again predicted by a peak in the SH derived deposits. In contrast, the second deposit peak, at L/D ≈ 110, does not appear to coincide with either a local zone of oxygen depletion or a peak in surface temperature. The cause of this second deposit peak could be due to either chemical or physical effects. As described previously, physical deposit processes can include: agglomeration of bulk deposit precursors, transport of these precursors to the surface, and finally precursor coalescence onto the surface. Additionally, high temperature oxidation reactions, that have not been previously observed, could be taking place under these severe thermal conditions. High temperature oxidation of the fuel and/or deposit precursors could lead to undiscovered deposition pathways. The idea of a high temperature, oxidative deposition route could be supported by the observation that the current chemical model under predicts the bulk oxygen consumption, even though the predicted bulk temperature is higher than the measured value (Table 13). Regardless, it is clear that additional study on oxidation and deposition kinetics is required in this unique regime of high heat flux.

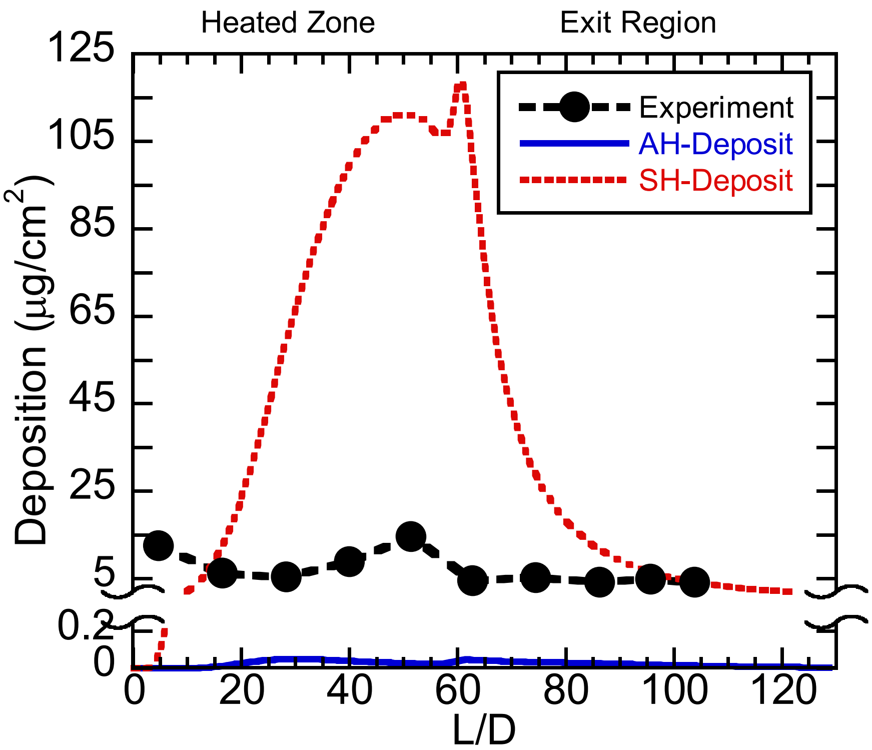

Figure 24. Measured carbon deposits (markers), simulated AH surface deposits (solid blue curve), and simulated SH surface deposits (dotted red curve) for Case A.

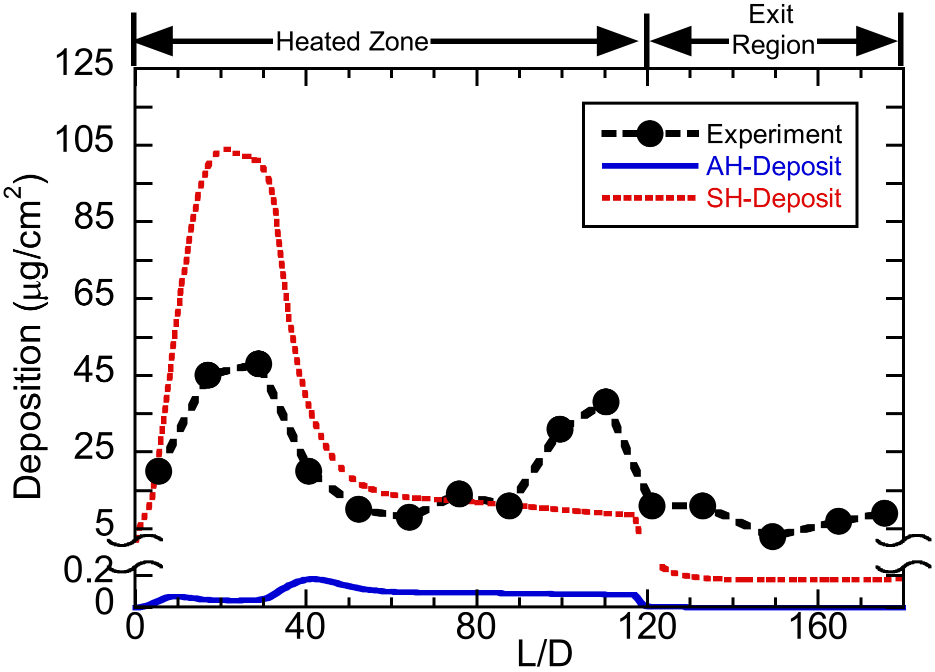

Figure 25. Measured carbon deposits (markers), simulated AH surface deposits (solid blue curve), and simulated SH surface deposits (dotted red curve) for Case B.

CHAPTER V

CONCLUSIONS

Summary

The experimental measurements of hydroperoxide decomposition for conditions relevant to liquid phase jet fuel autoxidation have been reported. The unimolecular decomposition of hydroperoxide was shown to closely fit first order behavior with respect to the hydroperoxide concentration. The first order behavior occurred for a range of three different hydroperoxides: cumene hydroperoxide (CHP), dodecane hydroperoxide (DHP), and ethylbenzene hydroperoxide (EBHP). The activation energy for liquid phase hydroperoxide decomposition was shown to be about 20 kcal/mol lower than the gas phase activation energy, which is primarily attributed to cage effects in the liquid phase. Addition of dissolved metal increases the decomposition rate of hydroperoxide; however, this effect is dependent upon the metal type and ligand type. Cu and Mn were shown to be very reactive, while Fe and Zn were less reactive elements. The addition of naphthenic acids (NA) alone was shown to have little effect on the hydroperoxide decomposition rate; however, the combination of NA and dissolved metal proved to synergistically increase the rate of hydroperoxide decomposition. Also, it was shown that metal deactivator additive (MDA) can effectively inhibit the increased hydroperoxide decomposition rate due to dissolved Cu, even in the presence of NA.

Experiments in jet fuel deposition, in which hydroperoxide decomposition pathways were isolated, show that this reaction pathway results in deposit formation which is catalyzed by the presence of Cu. Naphthenic acids were also found to catalyze deposit formation reactions during hydroperoxide decomposition. MDA was found to slow deposition rates in the presence of Cu, acid, or the combination of the two.

Experiments investigating the effects of high flux heat transfer on jet fuel were also reported. High outer wall temperatures, ≥ 600°C, were recorded while bulk exit temperatures were as low as 65°C. CFD with chemistry was used to model the flow conditions of both a laminar and a transitional flow heat transfer experiment. Due to the high heat flux conditions of these experiments, large radial temperature gradients were formed within the fluid flow. These large temperature gradients gave rise to localized points of oxygen depletion near the wall, yet only low levels of bulk oxygen consumption were realized. Chemical kinetic rate parameter measurements from the hydroperoxide decomposition studies were incorporated into a revised pseudo-detailed chemical mechanism and used for chemical predictions. Intermediate species, such as hydroperoxides, showed variable concentrations in both the axial and radial dimensions depending on the localized net rate of generation. In addition, CFD with chemistry allowed spatial resolution of reaction rates within the fluid flow. The computations have shown that not all reactions reach a maximum rate in the same location – such as the hottest portion of the fuel – rather reaction rates are dependent upon many factors. These factors include concentration and temperature, which in turn are effected by geometry, flow conditions, other chemical reaction rates, and heat transfer conditions. Computations showed that transitioning from laminar to turbulent flow can contribute to enhanced reaction rates for some deposit precursor forming reactions. The deposition model was able to predict the location of some deposit peaks; however, additional model refinement is necessary to extend the applicable temperature range.

Recommendations

Fundamental chemistry of jet fuel autoxidation has been reported above and then applied to an advanced jet fuel cooling scheme using computational tools. While much was learned along the way, there are still many unanswered questions regarding jet fuel stability. The remaining discussion will address some of the more pressing questions and research opportunities regarding jet fuel stability; and then present a long-term vision for aviation turbine fuels.

Question #1: How can jet fuel deposition predictions be improved? Fundamental chemical kinetic studies, e.g., doping studies, should be conducted to isolate and examine the role various heteroatomic species classes have in deposition. Oxygenates and, to some extent, sulfur containing species have already been included in the current pseudo-detailed chemical model; however, nitrogen containing heteroatomic species and synergism(s) between heteroatomic species classes have not been taken into account. It is well known that nitrogen containing species play a role in jet fuel thermal stability, yet this knowledge has not been transitioned to real systems and/or design tools such as CFD with chemistry. The determination of deposition pathways will invariably involve the use of group type analysis techniques to identify and monitor influential trace/heteroatomic species classes.

The development of advanced analysis techniques is critical to understanding the influential species classes in jet fuel. Group type analysis, such as GC×GC and HPLC-

MS, which target trace chemical species classes must be improved and refined. As group type compositional information becomes more readily available for a variety of fuels more will be learned about what the underlying causes are for fit-for-purpose fuel properties, such as thermal stability. Additionally, fuel surveys that include more complete trace compositional information can be used as detailed databases for correlation. Detailed chemical information can be used directly to predict individual fuel thermal stability characteristics or composite/statistical information can be drawn from fuel survey databases to generate an average fuel composition for use in computational design tools.

Regardless, additional experiments need to be conducted to better define the kinetics of jet fuel deposition pathways. This includes the current sulfur based and phenolic based deposition pathways, as well as future pathways involving nitrogen or physical processes, e.g., solubility effects. These experiments should be performed over a variety of temperatures and fuel chemistries to encompass most current and future jet fuel thermal stress situations. It is important to expand and improve current composition based deposition models so that jet fuel stability can be more accurately predicted from simple compositional analysis. In order for predictive models to be useful to designers, the models must be accurate and robust.

Question #2: Can oxidation and pyrolysis both be relevant under similar reaction conditions? As was previously discussed, chemical reactions proceed as a function of not just temperature, but also time and concentration. Based on the high heat flux experiments reported in Chapter IV, it appears entirely possible that oxidation and pyrolysis reactions could occur in relatively close proximity, such that the two regimes could interact. The existence of high temperature oxidation pathways should be explored and kinetic parameters should be revised to include these high temperature regions. As future aircraft will demand advanced cooling schemes, the possibility for unique oxidation and pyrolysis chemistry interaction continues. Therefore, jet fuel stability experiments need to explore the oxidation/pyrolytic reaction space, where overlap may occur with high temperatures and short residence times. Experiments should determine if pyrolytic radical production affects autoxidation. Additionally, advanced jet fuel stability will inevitably include both oxidation and pyrolytic regimes; therefore, there is a need to combine both chemistries into a single, unified thermal stability model.

Future

Kerosene jet fuels will continue to play an important role in the future as an aircraft energy source and heat sink. However, for jet fuel to meet the stringent demands of future aircraft, we must adopt a philosophy of understanding these fuels rather than simply testing them. Performance based fuel tests can only keep up with current technologies. Understanding the chemical composition of a fuel, and how that composition affects fuel performance, is a much more empowered strategy towards efficient fuel use. Future research should involve detailed chemical analysis to develop a more complete picture of the relationship between composition and performance. It seems paramount not to forget the initial intentions of this fuels research set forth many decades ago: to develop an understanding of the causes of jet fuel stability/instability; how to measure and quantify these causes and effects; and finally, how to predict the stability of jet fuels. It is implicit that with this understanding of jet fuel stability comes the ability to avoid, mitigate, and prevent fuel system fouling, which can only serve to enhance aircraft design and operation.

BIBLIOGRAPHY

Air Force Petroleum Office. (2010). *Detail specification: Turbine fuel, aviation, kerosene type, JP-8 (NATO F-34), NATO F-35, and JP-8+100 (NATO F-37)* (Specification Report No. MIL-DTL-83133G). Wright-Patterson AFB, OH: AFPET.

ANSYS Incorporated. (2010a). *Fluent* (version 13) [computer software]. Canonsburg, PA: SAS IP, Inc.

ANSYS Incorporated. (2010b). *ANSYS FLUENT Theory Guide* (Release 13.0). Canonsburg, PA: SAS IP, Inc.

ASTM International. (2011). *Standard specification for aviation turbine fuels* (ASTM Designation: D1655-11a). West Conshohocken, PA: ASTM.

Bates, R., Edwards, T., & Meyer, M. L. (2002). Heat transfer and deposition behavior of hydrocarbon rocket fuels (AIAA Paper No. AIAA-2003-0123). *41st Aerospace Sciences Meeting and Exhibit*. Reno, NV: AIAA.

Beaver, B., Gao, L., Burgess-Clifford, C., & Sobkowiak, M. (2005). On the mechanisms of formation of thermal oxidative deposits in jet fuels. *Energy & Fuels*. 19, 1574-1579.

Benson, S. W. (1981). The kinetics and thermochemistry of chemical oxidation with application to combustion and flames. *Progress in Energy and Combustion Science*. 7, 125-134.

Benson, S. W. (1986). Combustion, a chemical and kinetic view. *21st International Symposium on Combustion*. Pittsburgh, PA: The Combustion Institute.

Chevron Products Company. (2007). *Aviation fuels technical review* (FTR-3). Houston, TX: Chevron Corporation.

Coordinating Research Council. (1963). *Anticipated fuel system environment for the supersonic transport* (CRC Report No. LD-125). New York: CRC Incorporated.

Coordination Research Council. (1979). *CRC literature survey on the thermal oxidative stability of jet fuel* (CRC Report No. 509). Atlanta, GA: CRC Incorporated.

Coordinating Research Council. (1991). *Survey of current aircraft engine conditions* (CRC Report No. 573). Alpharetta, GA: CRC Press.

Coordinating Research Council. (2004). *Handbook of aviation fuel properties* (3rd ed.) (CRC Report No. 635). Alpharetta, GA: CRC Press.

Curran, H. J., Gaffuri, P., Pitz, W. J., & Westbrook, C. K. (1998). A comprehensive modeling study of n-heptane oxidation. *Combustion and Flame.* 114, 149-177.

Davies, R. E. G. (2003). The world's first commercial jets (AIAA Paper No. 2003-2882). *AIAA/ICAS International Air and Space Symposium and Exposition.* Dayton, OH: AIAA.

Denisov, E. T. (1974). *Liquid-phase reaction rate constants*. New York: IFI/Plenum.

Denisov, E. T., & Denisova, T. G. (2000). *Handbook of antioxidants* (2nd ed.). New York: CRC Press.

Dieterle, G. L., & Binns, K. E. (1998). Evaluation of JP-8+100 additives in large laboratory test systems (AIAA Paper No. 98-3531). *34th AIAA/ASME/SAE/ASEE Joint Propulsion Conference & Exhibit.* Cleveland, OH: AIAA.

Dukek, W. G., Winans, D. R., & Ogston, A. R. (1969). Milestones in aviation fuels (AIAA Paper No. 69-779). *AIAA Aircraft Design and Operations Meeting*. Los Angeles, CA: AIAA.

Edwards, T. (2003). Liquid fuels and propellants for aerospace propulsion: 1903-2003. *Journal of Propulsion and Power*. 19(6), 1089-1107.

Edwards, T., Harrison, B., Zabarnick, S., DeWitt, M., & Bentz, C. E. (2004). Update on the development of JP-8+100 (AIAA Paper No. 2004-3886). *40th AIAA/ASME/SAE/ASEE Joint Propulsion Conference & Exhibit*. Fort Lauderdale, FL: AIAA.

Edwards, T., & Meyer, M. L. (2002). Propellant requirements for future aerospace propulsion systems (AIAA Paper No. 2002-3870). *38th AIAA/ASME/SAE/ASEE Joint Propulsion Conference & Exhibit.* Indianapolis, IN: AIAA.

Ervin, J. S., Ward, T. A., Williams, T. F., & Bento, J. (2003). Surface deposition within treated and untreated stainless steel tubes resulting from thermal-oxidative and pyrolytic degradation of jet fuel. *Energy & Fuels*. 17, 577-586.

Ervin, J. S., Williams, T. F., & Katta, V. R. (1996). Global kinetic modeling of aviation fuel fouling in cooled regions in a flowing system. *Industrial & Engineering Chemistry Research*. 35, 4028-4036.

Gao, F., Boyles, D., Sullivan, R., Compton, R. N., & Pagni, R. M. (2002). Photochemistry of racemic and resolved 2-iodooctane: Effect of solvent polarity and viscosity on the chemistry. *Journal of Organic Chemistry.* 67, 9361-9367.

Gardiner, W. C. (1972). *Rates and Mechanisms of Chemical Reactions.* London: W.A. Benjamin.

Gatlin, C. L., Turecek, F., & Vaisar, T. (1994). Determination of soluble Cu(I) and Cu(II) species in jet fuel by electrospray ionization mass spectrometry. *Analytical Chemistry.* 66, 3950-3958.

Giovanetti, A. J., & Szetela, E. J. (1985). Long term deposit formation in aviation turbine fuel at elevated temperature (NASA Report No. CR-179579). Washington, D.C.: NASA.

Hardy, D. R., & Wechter, M. A. (1994). Characterization of soluble macromolecular oxidatively reactive species (SMORS) from middle distillate diesel fuels: Their origin and role in instability. *Energy & Fuels*. 8, 782-787.

Hazlett, R. N. (1991). *Thermal Oxidation Stability of Aviation Turbine Fuels.* Philadelphia: ASTM.

Heiser, W. H., & Pratt, D. T. (1994). *Hypersonic Airbreathing Propulsion*. Washington, DC: AIAA.

Hitch, B. D., & Karpuk, M.E. (1997). Experimental Investigation of Heat Transfer and Flow Instabilities in Supercritical Fuels (AIAA Paper No. 97-3043). *33rd AIAA/ASME/SAE/ASEE Joint Propulsion Conference & Exhibit*. Seattle, WA: AIAA.

Hitch, B. D., & Karpuk, M.E. (1998). Enhancement of heat transfer and elimination of flow oscillations in supercritical fuels (AIAA Paper No. 98-3759*). 34th AIAA/ASME/SAE/ASEE Joint Propulsion Conference & Exhibit*. Cleveland, OH: AIAA

Hua, Y. X., Wang, Y. Z., & Meng, H. (2010). A numerical study of supercritical forced convective heat transfer of n-heptane inside a horizontal miniature tube. *Journal of Supercritical Fluids.* 52, 36-46.

Huber, M. L. (1999). *NIST Thermophysical Properties of Hydrocarbon Mixtures, SUPERTRAPP* (version 3.0) [computer software].Gaithersburg, MD: U.S. Department of Commerce.

Incropera, F. P., DeWitt, D. P., Bergman, T. L., & Lavine, A. S. (2007). *Fundamentals of Heat and Mass Transfer* (6th ed.). USA: Wiley.

Jiang, H. (2011). Effect of changes in flow geometry, rotation and high heat flux on fluid dynamics, heat transfer and oxidation/deposition of jet fuels. (Doctoral Dissertation). University of Dayton, Dayton, OH.

Jones, E. G., Balster, W. J., & Balster, L. M. (1996). Thermal stability of jet-A fuel blends. *Energy & Fuels.* 10, 509-515.

Jones, E. G., Balster, W. J., & Post, M. E. (1993). Degradation of a jet-A fuel in a single-pass heat exchanger (ASME Paper No. 93-GT-334). *International Gas Turbine and Aeroengine Congress and Exposition.* Cincinnati, OH: ASME.

Katta, V. R., Blust, J., Williams, T. F., & Martel, C. R. (1995). Role of buoyancy in fuel-thermal-stability studies. *Journal of Thermophysics and Heat Transfer.* 9(1), 159-168.

Katta, V. R., Jones, E. G., & Roquemore, W. M. (1998). Modeling of deposition process in liquid fuels. *Combustion Science and Technology.* 139, 75-111.

Katta, V. R., & Roquemore, W. M. (1993). Numerical method for simulating fluid-dynamic and heat-transfer changes in jet-engine injector feed-arm due to fouling. *Journal of Thermophysics and Heat Transfer*. 7(4), 651-660.

Kauffman, R. E. (1997). The effects of different sulfur compounds on jet fuel oxidation and deposition. *Journal of Engineering for Gas Turbines and Power*. 119, 322-327.

Kharasch, M. S., & Burt, J. G. (1951). The chemistry of hydroperoxides VIII: The acid-catalyzed decomposition of certain hydroperoxides. *Journal of Organic Chemistry*. 16, 150-160.

Kharasch, M. S., Fono, A., & Nudenberg, W. J. (1950). The chemistry of hydroperoxides I: The acid-catalyzed decomposition of α,α-dimethylbenzyl (α-cumyl) hydroperoxide. *Journal of Organic Chemistry*. 15, 748-752.

Kharasch, M. S., Fono, A., & Nudenberg, W. J (1951). The chemistry of hydroperoxides VI: The thermal decomposition of α-cumyl hydroperoxide. *Journal of Organic Chemistry*. 16, 113-127.

Klavetter, E. A., Martin, S. J., & Wessendorf, K. O. (1993). Monitoring jet fuel thermal stability using a quartz crystal microbalance. *Energy & Fuels*. 7, 582-588.

Kuprowicz, N. J. (2006). A predictive modeling approach to simulate liquid-phase oxidation and deposition of jet fuels. (Doctoral Dissertation). University of Dayton, Dayton, OH.

Kuprowicz, N. J., Ervin, J. S., & Zabarnick, S. (2004). Modeling the liquid-phase oxidation of hydrocarbons over a range of temperatures and dissolved oxygen concentrations with pseudo-detailed chemical kinetics. *Fuel*. 83, 1795-1801.

Kuprowicz, N. J., Zabarnick, S., West, Z. J., & Ervin, J. S. (2007). Use of measured species class concentrations with chemical kinetic modeling for the prediction of autoxidation and deposition of jet fuels. *Energy & Fuels*. 21, 530-544.

Linne, D. L., Meyer, M. L., Braun, D. C., & Keller, D. J. (2000). Investigation of instabilities and heat transfer phenomena in supercritical fuels at high heat flux and temperatures (AIAA Paper No. 2000-3128). Washington, D.C.: NASA.

Martel, C. R. (1987). Military jet fuels, 1944-1987 (AFSC Report No. AFWAL-TR-87-2062). Wright-Patterson AFB, OH: Air Force Systems Command, Air Force Wright Aeronautical Laboratories.

Menter, F. R. (1994). Two-equation eddy-viscosity turbulence models for engineering applications. *AIAA Journal*. 32(8), 1598-1605.

Mick, M. S. (1998). Fundamental studies of the oxidation and deposition of jet fuels. (Master Thesis). University of Dayton, Dayton, OH.

Morris, R. E., Evans, T., Hughes, J. M., Colbert, J. E., Kamin, R. A., & Nowack, C. J. (2005). Oxidation of JP-5 in single and multi-pass flow testing. *Proceedings of the 9th International Conference on Stability and Handling of Liquid Fuels.* Sitges, Spain: IASH.

Mushrush, G. W., Beal, E. J., Pellenbarg, R. E., Hazlett, R. N., Eaton, H. R., & Hardy, D. R. (1994). A model study of the thermal decomposition of cumene hydroperoxide and fuel instability reactions. *Energy & Fuels*. 8, 851-855.

Mushrush, G. W., Beal, E. J., Slone, E., & Hardy, D. R. (1996). Reaction of organosulfur compounds with naturally occurring peroxides in jet fuel. *Energy & Fuels*. 10, 504-508.

Naval Air Systems Command. (2004). *Detail specification: Turbine fuel, aviation, grades JP-4 and JP-5* (Specification Report No. MIL-DTL-5624U). Patuxent River, MD: NAVAIR.

Nurullina, N. M., Batyrshin, N. N., & Kharlampidi, Kh. E. (2006). Cumene hydroperoxide decomposition in the presence of organic zinc salts. *Petroleum Chemistry*. 46(5), 349-352.

Pande, S. G., Hardy, D. R., Kamin, R. A., Nowack, C. J., Colbert, J. E., Morris, R. E., & Salvucci, L. (2001). Quest for a reliable method for determining aviation fuel thermal stability: Comparison of turbulent and laminar flow test devices. *Energy & Fuels*. 15, 224-235.

Petrov, L. V., Solyanikov, V. M., & Denisov, E. (1977). Acid catalysis of homolytic decomposition of tert-butyl hydroperoxide in acetonitrile. *Russian Chemical Bulletin*. 26, 670-677.

Pizzarelli, M., Urbano, A., & Nasuti, F. (2010). Numerical analysis of deterioration in heat transfer to near-critical rocket propellants. *Numerical Heat Transfer, Part A*. 57(5), 297-314.

Pryor, W. A., & Smith, K. (1970). The viscosity dependence of bond homolysis: A qualitative and semiquantitative test for cage return. *Journal of the American Chemical Society*. 92(18), 5403-5412.

Ranzi, E., Dente, M., Goldaniga, A., Bozzano, G., & Faravelli, T. (2001). Lumping procedures in detailed kinetic modeling of gasification, pyrolysis, partial oxidation and combustion of hydrocarbon mixtures. *Progress in Energy Combustion and Science*. 27, 99-139.

Schwartz, F. G., & Eccleston, B. H. (1962). *Survey of research on the thermal stability of petroleum jet fuels* (Bureau of Mines Information Circular No. 8140). Washington, DC: United States Department of the Interior, Bureau of Mines.

Sebbar, N., Bockhorn, H., & Bozzelli, J. W. (2002). Structures, thermochemical properties (enthalpy, entropy and heat capacity), rotation barriers, and peroxide bond energies of vinyl, allyl, ethynyl and phenyl hydroperoxides. *Physical Chemistry Chemical Physics*. 4, 3691-3703.

Song, J. H., Kim, H. Y., Kim, H., & Bae, Y. Y. (2008). Heat transfer characteristics of a supercritical fluid flow in a vertical pipe. *Journal of Supercritical Fluids*. 44, 164-171.

Striebich, R. C., & Rubey, W. A. (1994). Analytical method for the detection of dissolved oxygen. *Proceedings from the 207th National Meeting of the American Chemical Society*. San Diego, CA: ACS Division of Petroleum Chemistry.

Taylor, D. B., & Synovec, R. E. (1994). Liquid chromatographic determination of copper speciation in jet fuel resulting from dissolved copper. *Journal of Chromatography, A.* 659, 133-141.

Taylor, W. F. (Ed.). (1979). Jet Fuel Thermal Stability (NASA Report TM-79231). Washington, D.C.: NASA.

Ward, T. A., Ervin, J. S., Zabarnick, S., & Shafer, L. (2005). Pressure effects on flowing mildly-cracked n-decane. *Journal of Propulsion and Power*. 21, 344-355.

Waynick, J. A. (2001). The development and use of metal deactivators in the petroleum industry: A review. *Energy & Fuels.* 15, 1325-1340.

West, Z. J., Adams, R. K., & Zabarnick, S. (2011). Homogeneous catalysis of liquid-phase hydroperoxide decomposition in hydrocarbons. *Energy & Fuels.* 25, 897-904.

West, Z. J., Zabarnick, S., & Striebich, R. C. (2005). Determination of hydroperoxides in jet fuel via reaction with triphenylphosphine. *Industrial & Engineering Chemistry Research.* 44, 3377-3383.

Yamagata, K., Nishikawa, K., Hasegawa, S., Fujii, T., & Yoshida, S. (1972). Forced convective heat transfer to supercritical water flowing in tubes. *International Journal of Heat and Mass Transfer*. 15, 2575-2593.

Zabarnick, S. (1994). Studies of jet fuel thermal stability and oxidation using a quartz crystal microbalance and pressure measurements. *Industrial & Engineering Chemistry Research.* 33, 1348-1354.

Zabarnick, S. (1998). Pseudo-detailed chemical kinetic modeling of antioxidant chemistry for jet fuel applications. *Energy & Fuels*. 12, 547-553.

Zabarnick, S., & Grinstead, R. R. (1994). Studies of jet fuel additives using the quartz crystal microbalance and pressure monitoring at 140°C. *Industrial & Engineering Chemistry Research.* 33, 2771-27777.

Zabarnick, S., & Phelps, D. K. (2006). Density functional theory calculations of the energetic and kinetics of jet fuel autoxidation reactions. *Energy & Fuels*. 20, 488-497.

APPENDIX A

GENERAL CONSERVATION EQUATIONS

ANSYS Fluent solves finite volume approximations of the below listed conservation equations (ANSYS, 2010b). The equations are written in cylindrical form for 2D axisymmetric flow, where z is the axial dimension, r is the radial dimension, $\boldsymbol{\delta}$ is a unit vector in the subscripted dimension, and the del operator takes the usual axisymmetric, cylindrical form:

$$\nabla = \boldsymbol{\delta_z} \frac{\partial}{\partial z} + \boldsymbol{\delta_r} \frac{\partial}{\partial r}.$$

A.1 Mass & Species Conservation

The continuity equation is given by:

$$\frac{\partial}{\partial z}(\rho v_z) + \frac{\partial}{\partial r}(\rho v_r) + \frac{\rho v_r}{r} = 0$$

Where,

v_z = axial velocity (m/s)
v_r = radial velocity (m/s)
ρ = density (kg/m^3)

The species transport equation is given by:

$$\nabla \cdot (\rho \vec{v} Y_i) = -\nabla \cdot \vec{\mathrm{J}}_\mathrm{i} + R_i$$

where,

Y_i = mass fraction of species i

$\vec{v}$ = overall velocity vector (m/s)

$\vec{\mathrm{J}}_{\mathrm{i}}$ = mass diffusion of species i

R_i = net rate of production of species i

The species transport equation is written for N-1 species, where N equals the total number of fluid species. Since the species mass fractions must sum to one, the N^{th} species mass fraction is determined as one minus the sum of the $N - 1$ solved mass fractions.

The mass diffusion, $\vec{\mathrm{J}}_{\mathrm{i}}$, and the net rate of production, R_i, are given by the following equations:

$$\vec{\mathrm{J}}_{\mathrm{i}} = -\left(\rho\mathcal{D}_{\mathrm{i}} + \frac{\mu_{\mathrm{t}}}{\mathrm{Sc}_{\mathrm{t}}}\right)\nabla \cdot \mathrm{Y}_{\mathrm{i}}$$

$$R_i = MW_i \sum_{j=1}^{N_R}\left(n_{i,j}k_j \prod_{s=1}^{N_S}[C_s]^{\eta_{s,j}}\right)$$

Where,

$\mathcal{D}_i$ = mass diffusion coefficient for species i (m^2/s)

μ_{t} = turbulent viscosity (cP)

Sc_{t} = turbulent Schmidt number

MW_i = molecular weight of species i (kg/kmol)

j = index variable for reaction number 1, 2, 3...N_R

N_R = total number of reactions

$n_{i,j}$ = stoichiometric coefficient of species i for reaction number j

k_j = reaction rate constant for reaction number j (kmol, m^3, s)

s = index variable for species number 1, 2, 3...N_s

N_s = total number of species

C_s = concentration of species s in reaction j (kmol/m^3)

$\eta_{s,j}$ = rate exponent for product species j in reaction s

The Arrhenius rate constant follows:

$$k_j = \mathrm{A_j} e^{-E_{a,j}/RT}$$

Where,

A_j = Arrhenius pre-exponential factor (kmol, m^3, s)
$E_{a,j}$ = activation energy (J/kmol)
R = universal gas constant (J/kmol-K)
T = absolute temperature (K)

A.2 Energy Conservation

The energy conservation equation is given by:

$$\nabla \cdot \left(\vec{v}(\rho E + \rho)\right) = \nabla \cdot \left(k_{eff} \nabla T\right) + S_h$$

Where,

k_{eff} = effective conductivity (W/m-K)
S_h = volumetric heat source (W/m^3)
E = total energy (J)

A.3 Momentum Conservation

The axial momentum conservation equation is given by:

$$\frac{1}{r}\frac{\partial}{\partial z}(r\rho v_z^2) + \frac{1}{r}\frac{\partial}{\partial r}(r\rho v_r v_z) = -\frac{\partial p}{\partial z} + \frac{1}{r}\frac{\partial}{\partial z}\left[r\mu\left(2\frac{\partial v_z}{\partial z} - \frac{2}{3}(\nabla \cdot \vec{v})\right)\right] + \frac{1}{r}\frac{\partial}{\partial r}\left[r\mu\left(\frac{\partial v_z}{\partial r} + \frac{\partial v_r}{\partial z}\right)\right] + \rho g_z$$

And the radial momentum conservation equation is given by:

$$\frac{1}{r}\frac{\partial}{\partial z}(r\rho v_z v_r) + \frac{1}{r}\frac{\partial}{\partial r}(r\rho v_r^2)$$

$$= -\frac{\partial p}{\partial r} + \frac{1}{r}\frac{\partial}{\partial z}\left[r\mu\left(\frac{\partial v_r}{\partial z} + \frac{\partial v_z}{\partial r}\right)\right] + \frac{1}{r}\frac{\partial}{\partial r}\left[r\mu\left(2\frac{\partial v_r}{\partial r} - \frac{2}{3}(\nabla \cdot \vec{v})\right)\right]$$

$$- 2\mu\frac{v_r}{r^2} + \frac{2}{3}\frac{\mu}{r}(\nabla \cdot \vec{v})$$

Where,

μ = dynamic viscosity (cP)
g_z = gravitational acceleration (-9.8066 m/s^2)

A.4 Turbulence Conservation

The SST κ-ω turbulence model, developed by Menter (1994), solves the closed forms of the following two equations:

$$\frac{\partial}{\partial z_i}(\rho\kappa v_i) = \frac{\partial}{\partial z_j}\left(\Gamma_\kappa \frac{\partial \kappa}{\partial z_j}\right) + \tilde{G}_\kappa - Y_\kappa + S_\kappa$$

$$\frac{\partial}{\partial z_i}(\rho\omega v_i) = \frac{\partial}{\partial z_j}\left(\Gamma_\omega \frac{\partial \omega}{\partial z_j}\right) + G_\omega - Y_\omega + D_\omega + S_\omega$$

Where,

κ = turbulence kinetic energy (J/kg)
ω = specific dissipation rate (s^{-1})
Γ_κ and Γ_ω = effective diffusivity of κ and ω, respectively
$\tilde{G}_\kappa$ and G_ω = generation term for κ and ω, respectively
Y_κ and Y_ω = dissipation term for κ and ω, respectively
D_ω = cross-diffusion term
S_κ and S_ω = source terms for κ and ω, respectively

APPENDIX B

TABULATED PROPERTY DATA FOR JP-8 JET FUEL

Property data for a JP-8 jet fuel was generated using NIST SuperTrapp software (Table 14) for a petroleum fraction having an API gravity of 42.3 and an average boiling point of 207°C (Huber, 1999). The estimated critical properties for this petroleum fraction are $T_c = 400°C$, $P_c = 322$ psia, and $V_c = 0.0038$ m^3/kg with an accentric factor of 0.4371 and an estimated molecular weight of 163 g/mol. However, the data in Table 14 was generated for a system pressure of 800 psia, which gives a pseudo-critical temperature (T_{pc}) – the point at which the specific heat peaks to reach a local maximum – of about 500°C.

Table 14. Estimated Property Data for a JP-8 Jet Fuel (API Gravity = 42.3 and Avg. BP = 207°C) at 800 psia

Temperature (K)	Density, ρ (kg/m^3)	Specific Heat, Cp (kJ/kg-K)	Thermal Conductivity, k (W/m-K)	Viscosity, μ (cP)	Enthalpy, H (kJ/kg)
275	826.9	1.719	0.120	2.124	-400
300	809.5	1.826	0.117	1.395	-340
325	791.5	1.932	0.114	1.004	-276
350	773.1	2.035	0.111	0.764	-209
375	754.4	2.136	0.107	0.603	-140
400	735.3	2.235	0.104	0.488	-67
425	715.7	2.332	0.100	0.402	8
450	695.7	2.428	0.097	0.336	86
475	675.1	2.522	0.094	0.284	167

(Table 14. Continued)

Temperature (K)	Density, ρ (kg/m^3)	Specific Heat, Cp (kJ/kg-K)	Thermal Conductivity, k (W/m-K)	Viscosity, μ (cP)	Enthalpy, H (kJ/kg)
500	653.9	2.614	0.090	0.241	251
525	631.9	2.707	0.087	0.207	337
550	608.8	2.799	0.084	0.178	426
575	584.5	2.892	0.081	0.153	518
600	558.5	2.987	0.079	0.132	613
625	530.4	3.084	0.076	0.113	710
650	499.5	3.187	0.073	0.097	810
675	465.0	3.299	0.071	0.082	914
700	425.7	3.424	0.069	0.068	1,020
725	380.4	3.560	0.068	0.055	1,130
750	329.5	3.674	0.067	0.044	1,244
$T_{pc} \approx$ 775	279.2	3.701	0.066	0.036	1,360
800	237.6	3.647	0.066	0.030	1,476
825	206.9	3.574	0.066	0.027	1,590
850	184.7	3.523	0.067	0.026	1,703
875	168.2	3.497	0.069	0.025	1,815
900	155.4	3.489	0.071	0.024	1,927
925	145.1	3.490	0.073	0.024	2,040
950	136.5	3.498	0.074	0.023	2,152
975	129.3	3.509	0.076	0.023	2,266
1,000	123.1	3.521	0.078	0.023	2,379
1,025	117.6	3.534	0.080	0.023	2,493
1,050	112.7	3.545	0.082	0.023	2,608
1,075	108.4	3.555	0.084	0.024	2,723
1,100	104.5	3.564	0.085	0.024	2,838
1,125	100.9	3.571	0.087	0.024	2,954
1,150	97.6	3.575	0.088	0.024	3,070
1,175	94.6	3.577	0.090	0.024	3,186
1,200	91.8	3.577	0.091	0.024	3,302